



**HAL**  
open science

# Monte Carlo simulations of coupled body-and Rayleigh-wave multiple scattering in elastic media

Zongbo Xu, Ludovic Margerin, Dylan T Mikesell

► **To cite this version:**

Zongbo Xu, Ludovic Margerin, Dylan T Mikesell. Monte Carlo simulations of coupled body-and Rayleigh-wave multiple scattering in elastic media. *Geophysical Journal International*, inPress, 10.1093/gji/ggab370 . hal-03343661

**HAL Id: hal-03343661**

**<https://hal.science/hal-03343661>**

Submitted on 14 Sep 2021

**HAL** is a multi-disciplinary open access archive for the deposit and dissemination of scientific research documents, whether they are published or not. The documents may come from teaching and research institutions in France or abroad, or from public or private research centers.

L'archive ouverte pluridisciplinaire **HAL**, est destinée au dépôt et à la diffusion de documents scientifiques de niveau recherche, publiés ou non, émanant des établissements d'enseignement et de recherche français ou étrangers, des laboratoires publics ou privés.

# 1 Monte Carlo simulations of coupled body- and 2 Rayleigh-wave multiple scattering in elastic media

3 Zongbo Xu<sup>1,2</sup>, Ludovic Margerin<sup>3</sup> and T. Dylan Mikesell<sup>1</sup>

<sup>1</sup>*Environmental Seismology Laboratory, Department of Geosciences, Boise State University, Boise, ID, USA.*

<sup>2</sup>*now at Université de Paris, Institut de physique du globe de Paris, CNRS, F75005 Paris, France.*

<sup>3</sup>*Institut de Recherche en Astrophysique et Planétologie, Observatoire Midi-Pyrénées, Université Paul Sabatier, CNRS, CNES, 14 Avenue Edouard Belin, 31400 Toulouse, France.*

4

## 5 **SUMMARY**

6 Seismic coda waves are commonly used in estimation of subsurface Q values and  
7 monitoring subsurface changes. Coda waves mainly consist of multiply scattered  
8 body and surface waves. These two types of waves interact with each other in the  
9 multiple scattering process, which thus leads to a spatiotemporal evolution of the  
10 body- and surface-wave energies. One cannot characterize the evolution because one  
11 has not fully understood the multiple scattering of the two types of waves. Thus one  
12 commonly assumes only one type of waves exists or ignores their interaction while  
13 studying the coda waves. However, neglecting the interaction leads to an incorrect  
14 energy evolution of the two types of waves and consequently biases the Q estima-  
15 tion or interpretation of coda-wave changes for monitoring. To better understand  
16 the interaction between these waves during multiple scattering and to model the en-  
17 ergy evolution correctly, we propose a Monte Carlo algorithm to model the multiple  
18 scattering process. We describe the physics of the scattering for the two types of  
19 waves and derive scattering properties like cross sections for perturbations in elas-  
20 tic properties (e.g. density, shear modulus and Lamé parameters). Our algorithm

incorporates this knowledge and thus physically models the body- and surface-wave energy evolution in space and time. The energy partitioning ratios between surface and body waves provided by our algorithm match the theoretical prediction based on equipartition theory. In the equipartition state, our simulation results also match Lambert’s cosine law for body waves on the free surface. We discuss how the Rayleigh-to-body-wave scattering affects the energy partitioning ratios. Our algorithm provides a new tool to study multiple scattering and coda waves in elastic media with a free surface.

**Key words:** Wave scattering and diffraction; Coda waves; Computational seismology; Surface waves and free oscillations.

## 1 INTRODUCTION

Coda waves are arrivals after direct waves in seismic recordings or seismic crosscorrelations. One commonly uses coda waves to investigate and monitor the subsurface. By studying coda waves from an earthquake event, one can estimate subsurface Q values (e.g. Aki & Chouet 1975). One can also compare the coda waves in two event recordings and estimate differences in the coda-wave arrival times (e.g. Poupinet et al. 1984; Snieder et al. 2002; Mikesell et al. 2015) or waveforms (e.g. Larose et al. 2010). This method is called coda wave interferometry (CWI) monitoring. By assuming the two events share a similar source location and focal mechanism, one can qualitatively conclude that these differences are due to small changes of seismic properties (e.g. density) in the subsurface (e.g. Snieder 2006). This monitoring method has been applied to repeated event data in nature (e.g. Grêt et al. 2005) and in the lab (e.g. Larose et al. 2010). This method is also commonly applied to the coda waves in seismic crosscorrelations to monitor things such as the seasonal subsurface variations (e.g. Sens-Schönfelder & Wegler 2006; Wang et al. 2017), volcanic eruptions (e.g. Brenguier et al. 2007, 2008), ice sheet melting (e.g. Mordret et al. 2016) or the groundwater transport (e.g. Clements & Denolle 2018). One can further quantitatively image small changes in the subsurface from the CWI monitoring results (i.e. coda-wave differences) using the physics of coda waves (e.g. Pacheco & Snieder 2005; Planès et al. 2015; Margerin et al. 2016).

One routinely utilizes multiply scattered waves in the coda waves in both attenuation and CWI monitoring studies. *Multiply scattered* implies that these waves have scattered more than once in the subsurface while propagating from a (virtual) source to a receiver. In mod-

52 elling multiply scattered waves, one rarely uses wave equation solvers because the simulation  
 53 requires so many simulation steps that both the computation cost and simulation result stor-  
 54 age are prohibitively expensive. An alternative to the full-wavefield simulation is radiative  
 55 transfer theory, which can be used to model the spatiotemporal evolution of the seismic wave  
 56 energy/envelope (e.g. Wu 1985; Weaver 1990; Ryzhik et al. 1996). In the case of coupled elas-  
 57 tic P and S waves, there exist semi-analytical solutions for the radiative transfer equations  
 58 in homogeneous media (e.g. Zeng 1993; Sato 1994), given the scattered-wave amplitudes are  
 59 isotropic. For inhomogeneous media and/or anisotropic scattering, one can adopt a Monte  
 60 Carlo simulation approach to solve the radiative transfer equations numerically (e.g. Gusev  
 61 & Abubakirov 1987; Hoshiya 1995, 1997). Furthermore, when using this approach, one only  
 62 needs to know the properties of scattering (e.g. scattered-wave amplitudes and mean free  
 63 paths) without explicitly referring to the radiative transfer equations (e.g. Margerin et al.  
 64 1998; Sanborn et al. 2017).

65 Most research on the radiative transfer theory so far has focused on either body or surface  
 66 waves, but neglected the interaction between the two. However, both body and surface waves  
 67 are present during the scattering process and they convert to one another via scattering (e.g.  
 68 Maeda et al. 2008). Thus the energy ratio between the two types of waves evolves in time  
 69 and space. Furthermore, Obermann et al. (2013) and Obermann et al. (2016) reveal that  
 70 these two waves possess different sensitivities to subsurface elastic parameters through full  
 71 wavefield simulations. Therefore, it is necessary to characterize the spatiotemporal evolution  
 72 of the energy partitioning ratio between body and surface waves, so that one can estimate  
 73  $Q$  accurately or physically interpret the monitoring results (i.e. coda-wave differences). In  
 74 current practice, one empirically assumes the energy ratios (e.g. Obermann et al. 2019) or  
 75 ignores one of the two types of waves (e.g. Sens-Schönfelder & Wegler 2006; Mainsant et al.  
 76 2012; Obermann et al. 2015).

77 There have been previous attempts to incorporate the coupling between surface and body  
 78 waves within a radiative transfer framework. To incorporate this coupling into the radiative  
 79 transfer equations, Tregoures & Van Tiggelen (2002) considered body, Rayleigh, and Lamb  
 80 waves in an elastic plate with a free surface boundary condition on each surface (top and  
 81 bottom), where Rayleigh and Lamb waves are both a mixture of elastic body (P and S) waves;  
 82 Borcea et al. (2021) approximated surface waves with acoustic waves trapped in a thin layer  
 83 of an acoustic two-layer plate bounded by reflecting surfaces at the top and bottom. In both  
 84 approaches the body waves cannot leak away at depth, which is not realistic for most Earth  
 85 applications. Zeng (2006) introduced radiative transfer equations for coupled surface and body

86 waves by simplifying the coupling. However, these approximations and the simplification are  
 87 hard to justify entirely from first principles. Margerin et al. (2019) extended the conventional  
 88 radiative transfer equation by incorporating the coupling between surface and body waves  
 89 in the context of the Helmholtz equation with an impedance-type boundary condition. As  
 90 Margerin et al. (2019) used the scalar Helmholtz equation, only one type of body wave exists  
 91 in their treatment. Based on the Born approximation, Margerin et al. (2019) derived the  
 92 scattering mean free times for surface and body waves in a homogeneous velocity model with  
 93 uniformly distributed point scatterers. Margerin et al. (2019) demonstrated that the surface-  
 94 wave scattering properties (e.g. mean free time) depend on depth, and they used a Monte  
 95 Carlo simulation to model the energy coupling between surface and body waves. However, a  
 96 significant shortcoming is that different types of body (P and S) waves can not be incorporated  
 97 into the simulation, because the simulation is based on the scalar equation. To overcome that  
 98 limitation, we take advantage of Maeda et al. (2008) who theoretically described the scattering  
 99 process between body and surface waves in detail. Based on these results, we derive key  
 100 scattering properties (e.g. cross sections and mean free time/path, Section 2), and then we use  
 101 these properties to develop a Monte Carlo simulation algorithm (e.g. Hoshiya 1991; Margerin  
 102 et al. 2000) to model the body- and Rayleigh-wave multiple scattering process (Section 3).  
 103 We focus on perturbations in density ( $\rho$ ), where these perturbations ( $\delta\rho$ ) act as scatterers in  
 104 the media. One could extend our simulation algorithm to perturbations of P-wave and S-wave  
 105 velocities using Birch's Law. We conduct the simulation with and without a P-S coupling  
 106 free-surface boundary condition and then estimate the temporal energy ratios from multiply-  
 107 scattered Rayleigh and body waves (Section 4). The temporal energy ratios eventually reach  
 108 steady values, i.e. equipartition ratios. We verify the simulation by comparing the equipartition  
 109 ratios to theoretical equipartition predictions. We finally discuss how to improve this algorithm  
 110 (Section 5). Our algorithm can improve coda-wave studies about attenuation and the use of  
 111 CWI for monitoring.

## 112 2 THE SCATTERING PROCESS

113 Knowledge of body- and Rayleigh-wave scattering processes is central for the radiative transfer  
 114 theory and Monte Carlo simulations. For example, in an elastic medium, there is body wave  
 115 to Rayleigh wave scattering denoted here as BR scattering. We consider three types of body  
 116 waves: P, Sv and Sh waves. Thus we have three types of BR scattering: PR, SvR and ShR.  
 117 Following the same logic, there is also Rayleigh wave to body wave (RB: RP/RSv/RSh),  
 118 Rayleigh wave to Rayleigh wave (RR) and body wave to body wave (BB such as PP, PSv

and PSh) scattering. For all of these scattering cases, we present the single scattering cross sections (i.e. the ratio of scattered wave energy to the incident wave energy flux) and the multiply scattering mean free path/time (which indicates how efficiently the incident wave energy will be scattered). All the equations in this study are presented in the frequency domain. Different Fourier transform conventions do not affect our equations, because the conventions mainly impact the sign of phase while we focus on energy transport in this study.

## 2.1 Wave intensity

Wave intensity is normally used to measure the energy flux density of a wave, and the intensity is the base for calculating the wave scattering properties known as cross section and mean free path/time. The intensity of an incident P wave in a homogeneous medium is

$$I^P(\omega) = \rho_0 \alpha_0 \omega^2 |A^{0P}|^2, \quad (1)$$

where  $\rho_0$  is the medium density,  $\alpha_0$  is the P-wave velocity,  $\omega$  is the angular frequency and  $A^{0P}$  is the incident P-wave displacement amplitude (Aki & Richards 2002). The P-wave displacement amplitude is a function of frequency and we only focus on one frequency (i.e.  $\omega$ ) here. Similarly, the intensity of a S wave is

$$I^S(\omega) = \rho_0 \beta_0 \omega^2 |A^{0S}|^2, \quad (2)$$

where the S wave can be either Sv or Sh and  $\beta_0$  is the S-wave velocity. We set the polarization direction for the incident Sh wave ( $\mathbf{e}^{Sh}$ ) as the y-axis direction ( $[0,1,0]$ ) in the following examples for simplicity (Figure 1). The units of  $I^P$  and  $I^S$  are both  $J/(m^2s)$ , where  $J$  represents the unit of energy, Joule.

The intensity of a Rayleigh wave is different from a body wave because a Rayleigh wave propagates along the surface with depth-dependent displacements. Thus the intensity of a Rayleigh wave is defined with a depth integral as (Aki & Richards 2002)

$$I^R(\omega) = \rho_0 U_R \omega^2 (A^{0R})^2 \int_0^\infty [r_1^2(z, \omega) + r_2^2(z, \omega)] dz, \quad (3)$$

where  $U_R$  is the Rayleigh-wave group velocity at the frequency  $\omega$ ,  $A^{0R}$  is the Rayleigh-wave amplitude, and  $r_1$  and  $r_2$  are the horizontal and vertical displacement eigenfunctions of the Rayleigh wave (Appendix A). The eigenfunctions vary with the depth and frequency. For brevity, we write this integral as  $\int (r_1^2 + r_2^2) dz$ . Notice that the units of  $I^P$  ( $I^S$ ) and  $I^R$  are  $J/(m^2s)$  and  $J/(ms)$ , respectively. The unit difference is due to the depth integral. We demonstrate how this difference affects our analysis of Rayleigh-wave scattering in the following section.

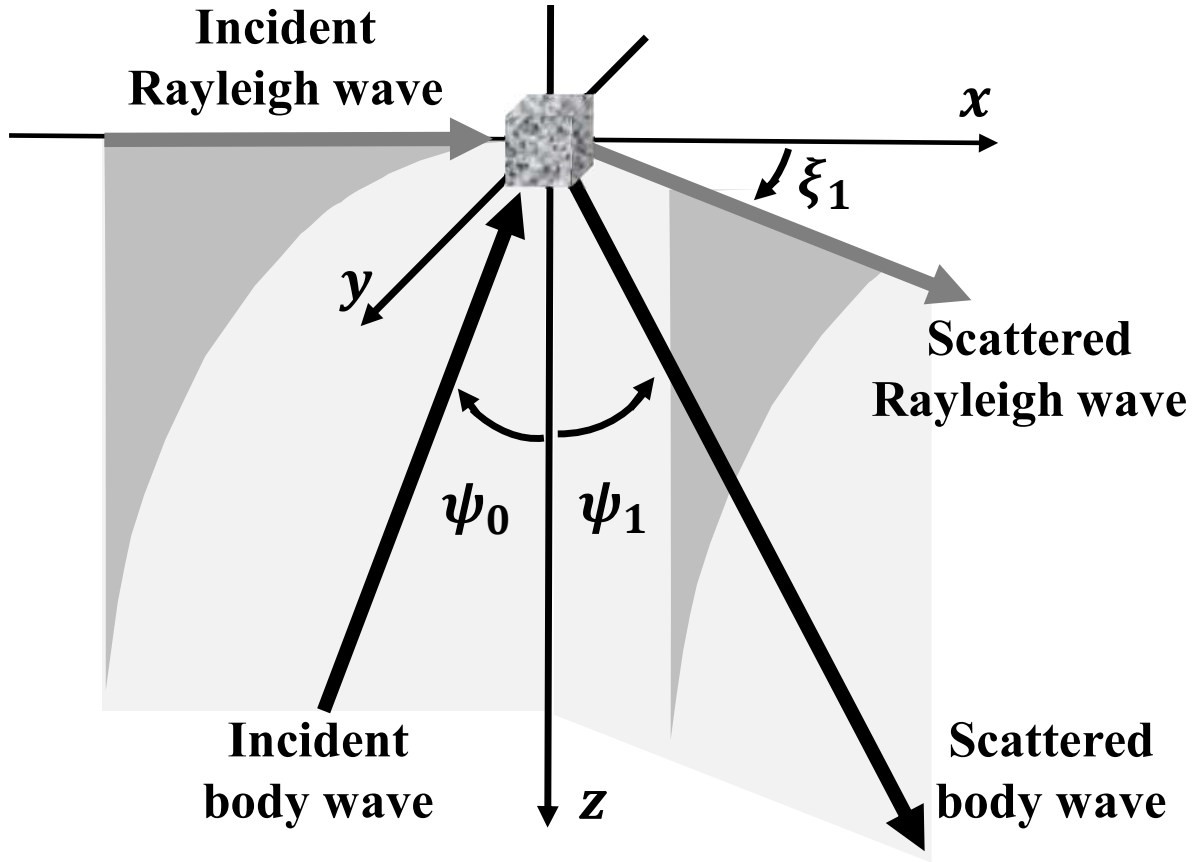


**Figure 1.** An illustration of single scattering process. The block is the scatterer. The thin black arrows represent local coordinate system. The thick black arrows are body waves. The gray arrows are Rayleigh waves. The gray shapes below the gray arrows represent the Rayleigh-wave eigenfunctions which decrease with depth increasing.

## 147 **2.2 Single scattering**

148 The scattering cross section is defined for a single scattering, in which an incoming wave  
 149 encounters a scatterer, as the ratio between the energy radiated by the scatterer in all out-  
 150 going propagation directions and the energy flux of the incoming wave. This ratio measures  
 151 the efficacy of the single scattering process. In elastic media, we need to calculate the cross  
 152 section for four types of single scattering: BR, RB, RR and BB. Calculation of each cross  
 153 section requires the corresponding scattering amplitude (e.g. Margerin et al. 2000). We use  
 154 the scattering amplitudes derived by Maeda et al. (2008) based on the Born approximation.  
 155 We consider scattering related to Rayleigh waves as an example in this section.

## 156 2.2.1 BR scattering

157 The ShR indicates a scattered Rayleigh wave from an incident Sh wave and is an example of BR  
 158 scattering. The  $m$ -component amplitude of a scattered Rayleigh wave due to a perturbation  
 159 of density ( $\delta\rho$ ) at  $\mathbf{x}_s$  is

$$A_{m,\rho}^{ShR}(\mathbf{x}, \omega) = \int_V \sum_n G_{mn}(\mathbf{x}, \mathbf{x}_s, \omega) \omega^2 \delta\rho A_n^{0Sh} e_n^{Sh} d\mathbf{x}_s. \quad (4)$$

160  $e_n^{Sh}$  is the  $n$ -component of incident Sh wave polarization vector,  $[0,1,0]$  (Figure 1). Based on  
 161 the Born approximation, the incident Sh wave scattering at  $\delta\rho$  acts like a seismic source and  
 162 generates scattered Rayleigh waves (e.g. Snieder 1986a; Maeda et al. 2008). Thus Equation 4  
 163 is a convolution between the Rayleigh-wave Green's function and a source term ( $\omega^2 A_n^{0Sh} \delta\rho$ ).  
 164 The amplitude of the far-field Rayleigh-wave Green's function is

$$G_{mn}(\mathbf{x}, \mathbf{x}_s, \omega) = \frac{p_m(z, \omega) p_n^*(z_s, \omega)}{4c_R U_R \int \rho_0 (r_1^2 + r_2^2) dz} \sqrt{\frac{2}{\pi k_R \Delta}}, \quad (5)$$

165 where  $k_R = \omega/c_R$  and  $c_R$  is Rayleigh-wave phase velocity at frequency  $\omega$ .  $p_m$  is a projection  
 166 of the Rayleigh-wave eigenfunction ( $r_1$  or  $r_2$ ) in the  $m$  direction, like  $[r_1 \cos \xi_1, r_1 \sin \xi_1, ir_2]$ ,  
 167 where  $\xi_1$  (Figure 1) is the scattered Rayleigh-wave propagation azimuth taken from the in-  
 168 cident wave azimuth (Snieder 1986a; Maeda et al. 2008).  $\Delta$  is the scattered Rayleigh-wave  
 169 travel distance from  $\mathbf{x}_s$  to  $\mathbf{x}$  along Earth's surface.  $z_s$  is the depth of perturbation  $\delta\rho$  and  $\rho_0$  is  
 170 the unperturbed/background density of the medium. The units of  $\delta\rho$  and  $\rho_0$  are both  $kg/m^3$ .  
 171 The scalar product between the polarization vectors in Equation 4 ( $\sum_n p_n^* e_n^{0Sh}$ ) determines  
 172 the coupling between the incident Sh and scattered Rayleigh waves. As the incident Sh wave  
 173 only possesses a horizontal component in the  $y$  direction ( $n = 2$ ),  $\sum_n p_n^* e_n^{0Sh}$  becomes  $p_2^*$ , i.e.  
 174  $r_1 \sin \xi_1$ . We then rewrite Equation 4 as

$$A_{m,\rho}^{ShR}(\mathbf{x}, \omega) = A^{0Sh} \frac{\omega^2 p_m(z, \omega)}{4c_R U_R \int (r_1^2 + r_2^2) dz} \sqrt{\frac{2}{\pi k_R \Delta}} \int_V r_1(z_s, \omega) \sin \xi_1 \frac{\delta\rho}{\rho_0} d\mathbf{x}_s. \quad (6)$$

175 In Equation 6, we remark that the scattered Rayleigh-wave amplitude does not depend on the  
 176 incident Sh wave angle ( $\psi_0$ ). Instead, we observe that the Rayleigh-wave amplitude depends  
 177 on the Rayleigh-wave propagation azimuth ( $\xi_1$ ), and this observation offers physical insights  
 178 into the scattering process. For example, if the scattered Rayleigh wave follows the same  
 179 azimuth as the incident wave ( $\xi_1 = 0$ ), we have  $\sin \xi_1 = 0$  and as a consequence, the scattered  
 180 amplitude is 0, which implies the absence of the ShR conversion in the forward direction. This  
 181 result, sometimes termed as selection rule, fits our physical intuition. An incident Sh wave  
 182 with particle motion in  $y$  direction does not excite a Rayleigh-wave propagating in  $x$  direction

183 because the two directions are orthogonal; furthermore, among all azimuths, the strongest  
184 excitation of Rayleigh waves occurs in the Sh wave polarization direction, i.e. the y direction.

185 We next assume that the size of the density perturbation is negligible compared to the  
186 Rayleigh-wave wavelength and further simplify Equation 6. Thus, we are in the so-called  
187 Rayleigh scattering regime (e.g. Wu & Aki 1985) and can rewrite Equation 6 as

$$A_{m,\rho}^{ShR}(\mathbf{x}, \omega) = A^{0Sh} \frac{\omega^2 p_m(z, \omega)}{4c_R U_R \int (r_1^2 + r_2^2) dz} \sqrt{\frac{2}{\pi k_R \Delta}} r_1(z_s, \omega) \sin \xi_1 V \frac{\delta \rho}{\rho_0}, \quad (7)$$

188 where we define  $V = \int_V d\mathbf{x}_s$ , the volume of a single scatterer. We then calculate the total  
189 energy of all the scattered Rayleigh waves by integrating the intensity over all azimuths using  
190 a cylindrical surface (S) integral:

$$E_\rho^{ShR}(z_s, \omega) = \rho_0 U_R \omega^2 \int_S \sum_m |A_{m,\rho}^{ShR}|^2 \Delta d\xi_1 dz, \quad (8)$$

$$= \rho_0 \omega^5 \frac{[A^{0Sh} r_1(z_s, \omega)]^2}{8c_R U_R \int (r_1^2 + r_2^2) dz} V^2 \left( \frac{\delta \rho}{\rho_0} \right)^2, \quad (9)$$

191 where  $A_{m,\rho}^{ShR}$  is from Equation 7 and  $\int \sum_m |p_m|^2 dz / \int (r_1^2 + r_2^2) dz = 1$ . We observe that the  
192 total energy depends on the scatterer depth,  $z_s$ . Based on the definition of the scattering cross  
193 section, we write the ShR cross section as

$$\sigma_\rho^{ShR}(z_s, \omega) = \frac{E_\rho^{ShR}}{I^{Sh}} = \frac{\omega^3}{8\beta_0 c_R U_R \int (r_1^2 + r_2^2) dz} r_1^2(z_s, \omega) V^2 \left( \frac{\delta \rho}{\rho_0} \right)^2. \quad (10)$$

194 The unit for this cross section is  $m^2$ . Notice this cross section depends explicitly on the  
195 scatterer depth ( $z_s$ ) through the Rayleigh-wave eigenfunction,  $r_1$ . Following the same logic,  
196 we write cross sections for the remaining BR and BB scattering in Appendix B. In contrast  
197 to the BR scattering, the BB cross sections are independent of the scatterer depth.

### 198 2.2.2 RB scattering

199 We next calculate the cross sections for incident Rayleigh waves. Following the same steps as  
200 above, for example, we can write the RSh cross section due to  $\delta \rho$  as

$$\sigma_\rho^{RSh}(z_s, \omega) = \frac{E_\rho^{RSh}}{I^R} = \frac{\omega^4 r_1^2(z_s, \omega)}{8\pi \beta_0^3 U_R \int (r_1^2 + r_2^2) dz} V^2 \left( \frac{\delta \rho}{\rho_0} \right)^2. \quad (11)$$

201 Notice the unit for  $\sigma_\rho^{RSh}$  is  $m$ , instead of  $m^2$  like  $\sigma_\rho^{ShR}$ . This is because of the unit difference  
202 between  $I^R$  and  $I^{Sh}$  (Section 2.1). For future reference, we introduce the following depth  
203 integrated cross section:

$$\bar{\sigma}_\rho^{RSh}(\omega) = \int_0^\infty \sigma_\rho^{RSh} dz_s = \frac{\omega^4 \int r_1^2(z_s, \omega) dz_s}{8\pi \beta_0^3 U_R \int (r_1^2 + r_2^2) dz} V^2 \left( \frac{\delta \rho}{\rho_0} \right)^2, \quad (12)$$

204 where the cross section unit is  $m^2$ . The definition is valid for a uniform and random distribution  
 205 of point scatterers, where the scattering of Rayleigh waves is directly proportional to the  
 206 depth integrated cross section. Following the same logic, we write the other RB and RR cross  
 207 sections (Appendix B). Notice that, the averaged RB and averaged RR cross sections are both  
 208 independent of the scatterer depth.

### 209 2.3 Isotropic incident angle assumption

210 Some cross sections are dependent on the incident angle,  $\psi_0$  (Figure 1). For example, for a P  
 211 wave scattered to a Rayleigh wave, the incident P-wave particle motion projects on both the  
 212  $x$  and  $z$  directions unless the P wave propagates purely vertically or horizontally. Thus  $\sigma_\rho^{PR}$   
 213 depends on the incident angle ( $\psi_0$ ), and we derive the cross section by following the same  
 214 steps as in Section 2.2:

$$\sigma_\rho^{PR} = \frac{\omega^3}{8\alpha_0 c_R U_R \int (r_1^2 + r_2^2) dz} (r_1^2 \sin^2 \psi_0 + 2r_2^2 \cos^2 \psi_0) V^2 \left( \frac{\delta\rho}{\rho_0} \right)^2. \quad (13)$$

215 We observe that  $\frac{\omega^3}{8\alpha_0 c_R U_R \int (r_1^2 + r_2^2) dz}$  is very similar to  $\frac{\omega^3}{8\beta_0 c_R U_R \int (r_1^2 + r_2^2) dz}$  in ShR scattering  
 216 (Equation 10) except the different incident wave velocities. We write  $C = r_1^2 \sin^2 \psi_0 + 2r_2^2 \cos^2 \psi_0$   
 217 and note that this term, similar to  $r_1^2$  in Equation 10, determines the coupling between the  
 218 incident P and scattered Rayleigh waves. For example,  $\psi_0 = 0$  (a vertically incident P-wave)  
 219 and  $\psi_0 = \pi/2$  (a horizontally incident P-wave) lead to purely vertical ( $C = 2r_2^2$ ) and horizontal  
 220 ( $C = r_1^2$ ) coupling, respectively. Therefore the PR cross section dependence on  $\psi_0$  makes  
 221 intuitive sense. This phenomenon also exists in the SvR scattering (Appendix B).

222 Equation 13 explicitly indicates that the BR scattering involves the body-wave incident an-  
 223 gle. This involvement significantly complicates any simulation, especially the following Monte  
 224 Carlo simulation, because we need to calculate the BR cross section for a given incident angle  
 225 ( $\psi_0$ ) and use the new cross section to determine scattering Rayleigh-wave azimuths ( $\xi_1$ ). Fur-  
 226 thermore, numerical simulations (e.g. Paul et al. 2005) demonstrate that the incident angles  
 227 become evenly distributed on the unit sphere (i.e. isotropic) after a sufficiently large number of  
 228 scattering events. Thus, we can eliminate the incident angle dependence of the BR scattering  
 229 cross sections (e.g.  $\sigma_\rho^{PR}$ ) by averaging the cross sections over the incident angles ( $\psi_0$ ):

$$\tilde{\sigma}_\rho^{PR} = \frac{1}{\int_0^\pi \sin \psi_0 d\psi_0} \int_0^\pi \sigma_\rho^{PR} \sin \psi_0 d\psi_0 = \frac{\omega^3}{12\alpha_0 c_R U_R \int (r_1^2 + r_2^2) dz} (r_1^2 + r_2^2) V^2 \left( \frac{\delta\rho}{\rho_0} \right)^2. \quad (14)$$

230 Following the same process, we average other incident-angle dependent cross sections and  
 231 present the results in Appendix B.

## 2.4 Multiple scattering

The knowledge of single scattering is the building block for multiple scattering, since multiple scattering can be modeled as a series of single scattering events in wave propagation from a (virtual) source to a receiver. This connection between multiple scattering and single scattering is known as the independent scattering approximation (e.g. Lagendijk & Van Tiggelen 1996). In the approximation, we define a volume density of point scatterers ( $n$ , unit:  $m^{-3}$ ) and write the mean free path ( $l^w$ ) for an incident wave as

$$l^w = \frac{1}{n\sigma^w}, \quad (15)$$

where  $\sigma^w$  is the sum of all the possible single-scattering cross sections for the incident wave (e.g. Margerin et al. 2000), such as  $\sigma_\rho^{Sh}(z, \omega) = \sigma_\rho^{ShR}(z, \omega) + \sigma_\rho^{ShP}(\omega) + \sigma_\rho^{ShSv}(\omega) + \sigma_\rho^{ShSh}(\omega)$  in this study. The mean free path indicates the average distance between two scattering events (e.g. Hoshiya 1991) and has the unit of  $m$ . The mean free path also indicates the energy being scattered: a smaller mean free path means there will be more scattered wave energy in the media and vice versa. The corresponding mean free time ( $\tau^w$ ) is defined as

$$\tau^w = \frac{l^w}{v_w} = \frac{1}{n\sigma v_w}, \quad (16)$$

where  $v_w$  is the incident wave velocity (e.g. Margerin et al. 2000). The mean free time indicates the average time interval between scattering events. Notice that we will use a random variable called free time in the following Monte Carlo simulation (Section 3), and the free time is a time interval between two random scattering events. An important ingredient that differentiates our approach from Maeda et al. (2008) is that we allow the depth-dependent scattering properties for body waves (e.g.  $\sigma_\rho^{ShR}$  and  $\sigma_\rho^{Sh}$ ). This depth dependence is related to the coupling of body and Rayleigh waves.

## 2.5 Theoretical equipartition value

We can calculate the theoretical equipartition energy ratio between two types of multiply-scattered waves. For example, one can calculate the energy ratio between multiply-scattered P and S waves based on the scattering relationship between the two types of body waves (e.g. Weaver 1982). Following the reciprocity relationship in Margerin et al. (2019) and ignoring P-S coupling at the free surface, we write the equipartition energy ratio between multiply-

258 scattered body and Rayleigh waves as

$$\frac{\bar{\bar{E}}_R}{\bar{E}_P} = \int_0^\infty \frac{\tau_\rho^{RP}(\omega)}{\tau_\rho^{PR}(z_s, \omega)} dz_s = \int_0^\infty \frac{\sigma_\rho^{PR}(z_s, \omega) \alpha_0}{\sigma_\rho^{RP}(\omega) U_R} dz_s = \frac{\pi \alpha_0^3}{\omega c_R U_R}, \quad (17)$$

$$\frac{\bar{\bar{E}}_R}{\bar{E}_{Sv}} = \int_0^\infty \frac{\tau_\rho^{RSv}(\omega)}{\tau_\rho^{SvR}(z_s, \omega)} dz_s = \int_0^\infty \frac{\sigma_\rho^{SvR}(z_s, \omega) \beta_0}{\sigma_\rho^{RSv}(\omega) U_R} dz_s = \frac{\pi \beta_0^3}{\omega c_R U_R}, \quad (18)$$

$$\frac{\bar{\bar{E}}_R}{\bar{E}_{Sh}} = \int_0^\infty \frac{\tau_\rho^{RSh}(\omega)}{\tau_\rho^{ShR}(z_s, \omega)} dz_s = \int_0^\infty \frac{\sigma_\rho^{ShR}(z_s, \omega) \beta_0}{\sigma_\rho^{RSh}(\omega) U_R} dz_s = \frac{\pi \beta_0^3}{\omega c_R U_R}, \quad (19)$$

259 where  $\bar{\bar{E}}_R$  is the total Rayleigh-wave energy over the whole medium, and  $\bar{E}_P$  is an integral of P-  
 260 wave energy over a constant-depth plane and thus is the energy density at the depth. The body-  
 261 wave energy densities are homogeneous at all depths in the equipartition regime (Margerin  
 262 et al. 2019), and we validate this in Section 3.  $U_R$  is equal to  $c_R$  in a homogeneous isotropic  
 263 elastic medium, but this is not the case in heterogeneous media. The equipartition relationships  
 264 (Equation 17-19) hold not only for density perturbations, but also for perturbations in the  
 265 Lamé parameter and shear modulus (Appendix B).

266 It is not straightforward to combine mode conversion (i.e. P-Sv coupling) at the free sur-  
 267 face with the reciprocity relationship when one derives the equipartition ratios (e.g. Shapiro  
 268 et al. 2000). In order to consider the mode conversion, one needs to adopt another approach  
 269 also mentioned in Margerin et al. (2019), the density of state (DOS) formulation. We use den-  
 270 sity of state in the equipartition derivation and achieve the same equipartition ratios (Equa-  
 271 tions 17-19) in Appendix C. We emphasize that, in a statistically uniform elastic halfspace,  
 272 the equipartition ratios do not depend on the nature of the disorder.

### 273 3 MONTE CARLO SIMULATION

274 We simulate multiple scattering with a Monte Carlo method. The Monte Carlo simulation  
 275 method has been applied to multiply scattered acoustic/elastic body waves (e.g. Hoshiya 1991;  
 276 Margerin et al. 2000). We use this method to simulate multiply-scattered body and Rayleigh  
 277 waves in a statistically uniform isotropic elastic medium filled with point scatterers. The idea  
 278 underlying the Monte Carlo simulation is to simulate the propagation and scattering of wave  
 279 energy as a random walk for a particle and repeat the random walk  $N$  times independently  
 280 (Algorithm 1). After the  $N$  simulations, we count how many body and Rayleigh particles exist  
 281 at each time step and interpret the body and Rayleigh particle numbers as the body- and  
 282 Rayleigh-wave energy, respectively. Furthermore, by discretizing the 3D medium into a grid  
 283 and recording changes of the particle numbers at each grid cell with time, we estimate the  
 284 evolution of wave energy in time and space.

285 We divide one simulation process into four parts and introduce them separately. Before  
 286 the simulations start, we need to calculate the cross sections and the mean free times for all  
 287 possible types of scattering. For perturbations in density or shear modulus, P, Sv, Sh and  
 288 Rayleigh waves can all be generated during the scattering process; for perturbations in Lamé  
 289 parameter, only P and Rayleigh waves are generated by the scattering.

### 290 3.1 Initialization

291 We launch a particle at the source location in the beginning of one simulation. The particle  
 292 can be a body (P/Sv/Sh) or Rayleigh wave (Algorithm 2). We can model different source  
 293 mechanisms by changing initial wave types (e.g. Margerin et al. 2000) and propagation direc-  
 294 tions (i.e. azimuth and colatitude). For example, if the source is an explosion, we can set that  
 295 only P waves are generated at the source location. The P-wave initial azimuths are randomly  
 296 generated with a uniform probability distribution between 0 and  $2\pi$ , and the cosines of the  
 297 P-wave initial colatitudes are randomly generated from a uniform distribution between -1  
 298 and 1 (Algorithm 2). For a shear-force source like a fault, all types of waves are randomly  
 299 selected in proportions equal to their respective radiated energy. Based on the initial wave  
 300 type, we compute a random free time ( $T$ ) which indicates the travel time before the next  
 301 scattering happens. We will cover the details of free time in the next section (Section 3.2).  
 302 We also calculate the wave propagation vector  $(k_x, k_y, k_z)$  based on the propagation azimuths  
 303 and colatitudes.

### 304 3.2 Effective cross section and mean free time

305 The initialized particle propagates during the random free time  $T$ . We compute  $T$  as  $T =$   
 306  $-\tau^w \ln(rand)$  where  $rand$  is a random number with a uniform probability distribution from  
 307 0 to 1 (e.g. Hoshihara 1991), and  $w$  indicates a body ( $B$ ) or Rayleigh wave ( $R$ ). We directly  
 308 follow the computation for Rayleigh-wave free time but not for the body-wave. Calculation  
 309 of the body-wave free time between two scattering events is not straightforward, since the  
 310 body-wave mean free time ( $\tau^B$  e.g.  $\tau_\rho^{Sh}$ ) varies with depth (Section 2.4). This is because  
 311  $\tau_\rho^{Sh}$  is inversely proportional to  $\sigma_\rho^{Sh}$ , where  $\sigma_\rho^{Sh}$  includes the depth-dependent  $\sigma_\rho^{ShR}$ . Thus,  
 312 calculation of the body-wave free time requires tracking of the body-wave depth in order to  
 313 integrate the variation of the mean free time in the propagation. To address this difficulty, we  
 314 adopt a trick called delta collisions (Lux & Koblinger 1991). The idea of delta collisions is to  
 315 impose an effective and constant cross section ( $\sigma^{Be}$  where  $e$  stands for 'effective') and mean  
 316 free time. To compensate for the difference between  $\sigma^{Be}$  and the real cross section at a given

**Algorithm 1** Monte Carlo simulation algorithm

---

$\sigma^{Be} = \sum_{B'} \sigma^{BB'} + \max[\sigma^{BR}(z)]$  ▷ Calculating effective body-wave cross section  
▷  $B$  and  $B'$  can be any possible body wave in scattering, P, Sv or Sh.

$\tau^{Be} = 1/n/\sigma^{Be}/vb$  ▷ Effective body-wave mean free time

$\sigma^R = \sigma^{RR} + \sum_B \sigma^{RB}$  ▷ Rayleigh wave cross section

$\tau^R = 1/n/\sigma^R/vr$  ▷ Rayleigh wave mean free time

Set dt, the time step for recording particle numbers for each wave mode, P, Sv, Sh and R

**for**  $i = 1 : N$ th simulation **do**

[mode  $T$  azi0 kx ky kz] = Initialization() ▷ Wave mode, free time, propagation azimuth and vector

Set x, y and z at the source location

**while** itime < Nstep **do** ▷  $i$ th simulation starts

**if** mode == B **then** ▷ Body-wave propagation

**if**  $T > \text{deltat}$  **then** ▷ No scattering happen

$x = x + \text{deltat} * vb * kx$ ;  $y = y + \text{deltat} * vb * ky$ ;  $z = z + \text{deltat} * vb * kz$

**if**  $z < 0$  **then** ▷ Encounter the free surface

FreeSurfaceBoundaryCondition

itime = itime + 1 ▷ Record body-wave type at this time point

$T = T - \text{deltat}$

deltat = dt

**else** ▷ A scattering will happen

$x = x + T * vb * kx$ ;  $y = y + T * vb * ky$ ;  $z = z + T * vb * kz$

**if**  $z < 0$  **then** ▷ Encounter the free surface

FreeSurfaceBoundaryCondition

deltat = deltat -  $T$

[mode  $T$  azi0 kx ky kz] = scatterb(azi0) ▷ Body-wave scattering

**if** mode == R **then** ▷ Rayleigh-wave propagation

**if**  $T > \text{deltat}$  **then** ▷ No scattering happen

$x = x + \text{deltat} * vr * kx$ ;  $y = y + \text{deltat} * vr * ky$

itime = itime + 1 ▷ Record Rayleigh wave type at this time point

$T = T - \text{deltat}$

deltat = dt

**else** ▷ A scattering will happen

$x = x + T * vr * kx$ ;  $y = y + T * vr * ky$

deltat = deltat -  $T$

[mode  $T$  azi0 kz ky kz z] = scatterr(azi0) ▷ Rayleigh-wave scattering

---

---

**Algorithm 2** Simulation initialization: [mode  $T$  azi0 kx ky kz] = Initialization()

---

 Generate a particle; its **mode** can be a body (B = P/Sv/Sh) or Rayleigh (R) wave

**if** mode == B **then**
 $T = -\tau^{Be} * \ln(rand)$  ▷ Generate a random free time from a random number  
 $ang = \arccos(-1+2*rand)$  ▷ A random colatitude in  $[0, \pi]$   
 $azi0 = 2*\pi*rand$  ▷ A random propagation azimuth in  $[0, 2\pi]$   
 $kx = \sin(ang)*\cos(azi0)$  ▷ Body-wave propagation vector in Cartesian coordinates  
 $ky = \sin(ang)*\sin(azi0)$   
 $kz = \cos(ang)$ 
**else**
 $T = -\tau^R * \ln(rand)$   
 $azi0 = 2*\pi*rand$  ▷ A random propagation azimuth in  $[0, 2\pi]$   
 $kx = \cos(azi0)$  ▷ Rayleigh-wave propagation vector in Cartesian coordinates  
 $ky = \sin(azi0)$ 

 deltat = dt

---

317 depth, we introduce an imaginary scattering part into the body-wave scattering process. The  
 318 probability that the imaginary scattering event occurs is determined by the difference ( $1 - prs$   
 319 in Algorithm 3) between  $\sigma^{Be}$  and  $\sigma^B(z)$ . The imaginary scattering does not change the body-  
 320 wave propagation direction. Notice that we do not need to introduce the effective mean free  
 321 time for Rayleigh waves because both  $\bar{\sigma}^{RB}$  and  $\bar{\sigma}^{RR}$  (e.g. Equation 12) are independent of  
 322 depth.

### 323 3.3 Scattering

324 After propagating for time  $T$ , the particle encounters a scatterer/perturbation, and scattering  
 325 occurs. We generate a uniformly distributed random value in the range  $[0, 1]$  to simulate all  
 326 possible conversions and determine the scattered wave type (Algorithms 3 and 4). Notice that  
 327 for incident Rayleigh particles, if a RB conversion happens, we re-inject the scattered body  
 328 particle at a depth based on the distribution of  $\sigma^{RB}$  as a function of depth (Appendix D).  
 329 We generate the scattering azimuths and colatitudes ( $\xi_1$  &  $\psi_1$  in Section 2 or azi & ang in the  
 330 pseudocode) of scattered waves based on the probabilistic interpretation of scattering cross  
 331 sections (Appendix E). We add the scattering azimuths to the incident azimuth to achieve  
 332 the propagation azimuth. Due to the isotropic incident angle assumption (Section 2.3), we do  
 333 not need the incident angles in this part. We discuss this assumption in Section 5.1. Based on

334 the type of scattered wave, we generate a new value for  $T$  to determine the propagation time  
 335 before the next scattering event.

---

**Algorithm 3** Body-wave scattering subprogram: [mode  $T$  azi0 kx ky kz] = scatterb(azi0)

---

$\sigma^B(z) = \sigma^{BR}(z) + \sum_{B'} \sigma^{BB'}$   $\triangleright$  Cross section for all possible scattering at this depth

$prs = \sigma^B(z)/\sigma^{Be}$   $\triangleright$  Probability that scattering happening

**if**  $rand < prs$  **then**

    Generate a new random number,  $rand$   $\triangleright$  determine the scattered mode

**if**  $rand < \sigma^{BP}/\sigma^B(z)$  **then**  $\triangleright$  Possibility for BP scattering

        mode = P  $\triangleright$  scattered P wave,  $B' = P$

**if**  $\sigma^{BP}/\sigma^B(z) < rand < (\sigma^{BP} + \sigma^{BSv})/\sigma^B(z)$  **then**  $\triangleright$  Possibility for BSv scattering

        mode = Sv  $\triangleright$  scattered Sv wave,  $B' = Sv$

**if**  $(\sigma^{BP} + \sigma^{BSv})/\sigma^B(z) < rand < (\sigma^{BP} + \sigma^{BSv} + \sigma^{BSH})/\sigma^B(z)$  **then**

$\triangleright$  Possibility for BSv scattering

        mode = Sh  $\triangleright$  scattered Sh wave,  $B' = Sh$

$T = -\tau^{B'e} * \ln(rand)$   $\triangleright$  Generate a random free time from a new random number

    Generating azi and ang based on probability distributions (Appendix E)

    azi0 = azi0 + azi

    kx =  $\sin(ang) * \cos(azi0)$   $\triangleright$  Body wave propagation vector in Cartesian coordinates

    ky =  $\sin(ang) * \sin(azi0)$

    kz =  $\cos(ang)$

**if**  $(\sigma^{BP} + \sigma^{BSv} + \sigma^{BSH})/\sigma^B(z) < rand$  **then**  $\triangleright$  BR scattering

        mode = R

$T = -\tau^R * \ln(rand)$

        Generate azi based on probability distributions (Appendix E)

        azi0 = azi0 + azi

        kx =  $\cos(azi0)$   $\triangleright$  Rayleigh-wave propagation vector in Cartesian coordinates

        ky =  $\sin(azi0)$

**else**  $\triangleright$  Imaginary scattering happens

    mode = B

$T = -\tau^{Be} * \ln(rand)$   $\triangleright$  The propagation vector and direction stay the same

---

---

**Algorithm 4** Rayleigh-wave scattering subprogram: [mode  $T$  azi0 kx ky kz z] = scatterr(azi0)

```

zvec = 0 : Dz : zmax          ▷ The depth vector, from 0 to zmax, for injecting body wave
if rand <  $\sigma^{RR}/\sigma^R$  then                                ▷ RR scattering
    mode = R
     $T = -\tau^R * \ln(rand)$                                        ▷ Generate a random free time from a random number
    Generate azi based on probability distributions (Appendix E)
    azi0 = azi0 + azi
    kx = cos(azi0)           ▷ Rayleigh-wave propagation vector in Cartesian coordinates
    ky = sin(azi0)
else                                                                ▷ RB scattering
    if rand <  $(\sigma^{RR} + \sigma^{RP})/\sigma^R$  then
        mode = P                                                    ▷ RP scattering,  $B = P$ 
    if  $(\sigma^{RR} + \sigma^{RP})/\sigma^R < rand < (\sigma^{RR} + \sigma^{RP} + \sigma^{RSv})/\sigma^R$  then
        mode = Sv                                                  ▷ RSv scattering,  $B = Sv$ 
    if  $(\sigma^{RR} + \sigma^{RP} + \sigma^{RSv})/\sigma^R < rand$  then
        mode = Sh                                                  ▷ RSv scattering,  $B = Sh$ 
    z = interp1( $\sigma^{RB}(zvec)/\int \sigma^{RB}(z)dz, zvec, rand$ )
        ▷ Inject body wave at depth based on RB cross section in depth (Appendix D)
     $T = -\tau^{Be} * \ln(rand)$ 
    Generating azi and ang based on probability distributions (Appendix E)
    azi0 = azi0 + azi
    kx = sin(ang)*cos(azi0)   ▷ Body-wave propagation vectors in Cartesian coordinates
    ky = sin(ang)*sin(azi0)
    kz = cos(ang);

```

---

### 336 3.4 Boundary conditions

337 We assume the free surface is flat and adopt two types of free-surface boundary conditions  
338 (FSBCs) in the simulation: mirror-like reflection and mode conversion. The mirror FSBC con-  
339 serves the wave energy and propagation vector except for the sign of the vertical component.  
340 This FSBC does not modify the incident wave type (i.e. no mode conversion). The mode-  
341 conversion FSBC allows the wave mode conversion (i.e. P to Sv or Sv to P) based on energy  
342 reflection coefficients. Depending on the incident-wave angle and wave type (B=P/Sv), we  
343 can calculate the corresponding reflection coefficient ( $R_{BB}$ ) for a reflected wave remaining as  
344 the same wave type (e.g. Aki & Richards 2002, Chapter 5.2.2).  $R_{BB}$  is the reflected wave

345 amplitude ratio relative to the incident-wave amplitude. Given the incident-wave intensity is  
 346 1, we recognize that the square of the coefficient ( $R_{BB}^2$ ) is the intensity of the reflection wave  
 347 and the probability of this reflection. We then generate a random number from a uniform  
 348 distribution between 0 and 1. If the random number is less than or equal to  $R_{BB}^2$ , no mode  
 349 conversion happens; otherwise, the incident P or Sv wave will convert to a Sv or P wave, re-  
 350 spectively. If the mode conversion happens, we also recalculate the free time for the reflected  
 351 waves. For the boundary condition in the depth, we assume that body waves can propagate  
 352 to infinite depth in the simulations.

#### 353 4 SIMULATION RESULTS

354 We set the frequency be 1 Hz and choose the medium parameters as follows:  $\alpha_0=5$  km/s,  
 355  $\beta_0=3$  km/s and thus  $c_R=2.74$  km/s. We set the medium to be 10 km (zmax in Algorithm 4)  
 356 thick. We assume that there is no intrinsic attenuation in the medium, which means that the  
 357 seismic-wave energy will not irreversibly convert to other types of energies. We also assume  
 358 that the scatterers ( $\delta\rho$ ) are randomly distributed in the medium, and set the perturbation  
 359 density relative to the background ( $\delta\rho/\rho_0$ ) to 0.2 and a scatterer volume ( $V$ ) to be  $0.5\text{ m}^3$ . We  
 360 also set the volume density of scatterers ( $n$ ) equal to  $1\text{ m}^{-3}$ . We compute the Rayleigh-wave  
 361 eigenfunctions based on these velocities (Appendix A) and calculate all the cross sections and  
 362 mean free times (Appendix B and Equation 16). The Rayleigh-wave mean free path ( $l^R$ ) is  
 363 35.8 km (Equation 15) and is of the same order of mean free path as in Earth's crust (e.g.  
 364 Margerin et al. 1999). Note that the ratio between  $l^R$  and the Rayleigh-wave wavelength  
 365 (2.74 km) is 13 and fulfills the condition of application of radiative transfer theory that the  
 366 mean free path should be much larger than the corresponding wavelengths (e.g. Ryzhik et al.  
 367 1996). In the simulation, we place a source at 1 km depth. The source emits P and Rayleigh  
 368 waves/particles. During the random walk for one particle, we record the location and mode  
 369 for the particle every 1 s (dt in Algorithm 1). The random walk lasts 3000 s (Nstep=3000 in  
 370 Algorithm 1). We repeat the random walk 100 million ( $N = 10^8$ ) times. For each wave mode,  
 371 we count the particles in a certain space (e.g. the shallowest 1km depth of the medium) in all  
 372 the random walks and then divide the particle number with  $N$  to get the wave energy.

373 We first simulate multiple scattering with the mirror FSBC. At each time step in the  
 374 simulation, we estimate the body wave energy density as a function of depth ( $\overline{E}_B$ :  $\overline{E}_P$ ,  $\overline{E}_{Sv}$   
 375 and  $\overline{E}_{Sh}$ ) by counting the number of body waves per 1 km depth in the medium. We observe  
 376 that  $\overline{E}_B$  at each depth gradually becomes uniform in depth as the simulation time increases  
 377 (Figure 2). The homogenization of body-wave energy is due to the balance between the RB and

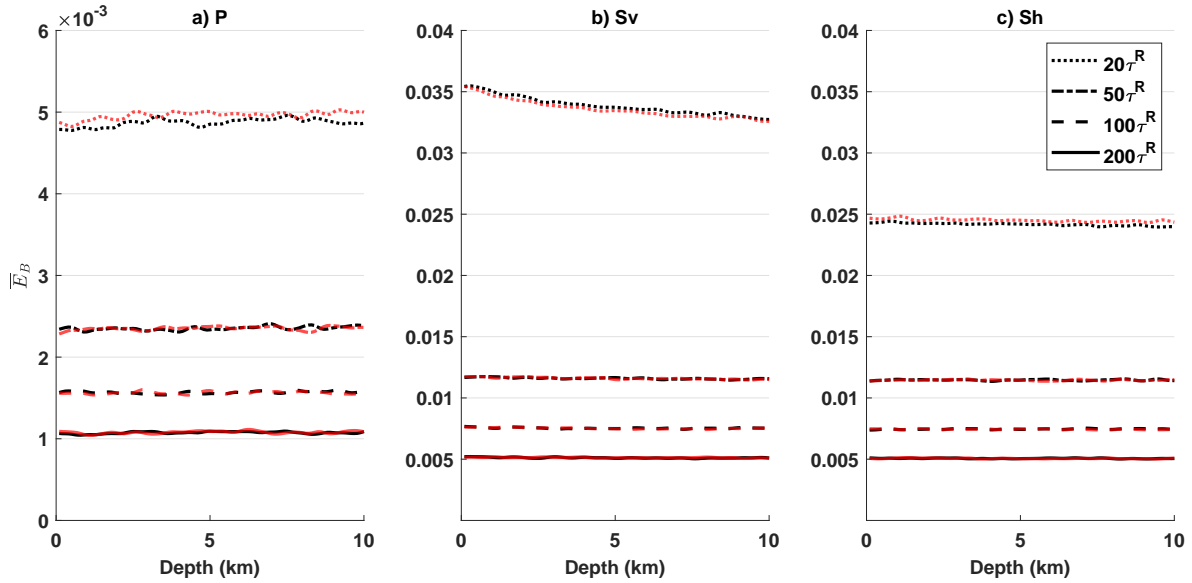


**Figure 2.** The simulated body-wave energy densities as a function of depth. We plot the energy densities at different simulation time in the unit of Rayleigh-wave mean free time ( $\tau^R$ ): 20, 50, 100 and 200  $\tau^R$ . The black curves are from the simulation with the mirror free surface boundary condition (FSBC); the red curves are from the mode-conversion FSBC. We smooth each curve by convolution with a Gaussian filter with a width of one third the Rayleigh-wave wavelength.

378 BR scattering (Margerin et al. 2019). We calculate the Rayleigh-wave energy ( $\overline{\overline{E}}_R$ ) by counting  
 379 the number of Rayleigh waves in the whole medium. We observe that the energy ratios between  
 380  $\overline{\overline{E}}_R$  and  $\overline{E}_{Sv/h}$  become homogeneous after 50  $\tau^R$ , and the energy ratios between  $\overline{\overline{E}}_R$  ( $\overline{E}_{Sv/h}$ )  
 381 and  $\overline{E}_P$  become constant after 100  $\tau^R$  (Figure 3). We determine that the simulation reaches  
 382 equipartition after all these energy ratios stabilize. All of the stable ratios are close to the  
 383 corresponding theoretical values with a 4.7% maximum misfit (Table 1).

384 We switch the FSBC to the mode-conversion case and repeat the simulation. In this  
 385 simulation, similar to the last one, we observe homogeneous body-wave energies in depth  
 386 in the equipartition stage (Figure 2). This mode-conversion FSBC provides similar energy  
 387 partition ratios among Rayleigh and body waves compared to the mirror FSBC simulation  
 388 (Figure 4 and Table 1). This similarity is not surprising because Trégourès & van Tiggelen  
 389 (2002) theoretically demonstrated that the mode-conversion (i.e traction free) FSBC does  
 390 not affect the body-wave energy partition ratios. Here we numerically demonstrate that no  
 391 matter which FSBC is used, the simulation reaches equipartition. In addition, the body-wave  
 392 angular distributions on the free surface match Lambert’s cosine law from the diffusion theory  
 393 (Appendix F).

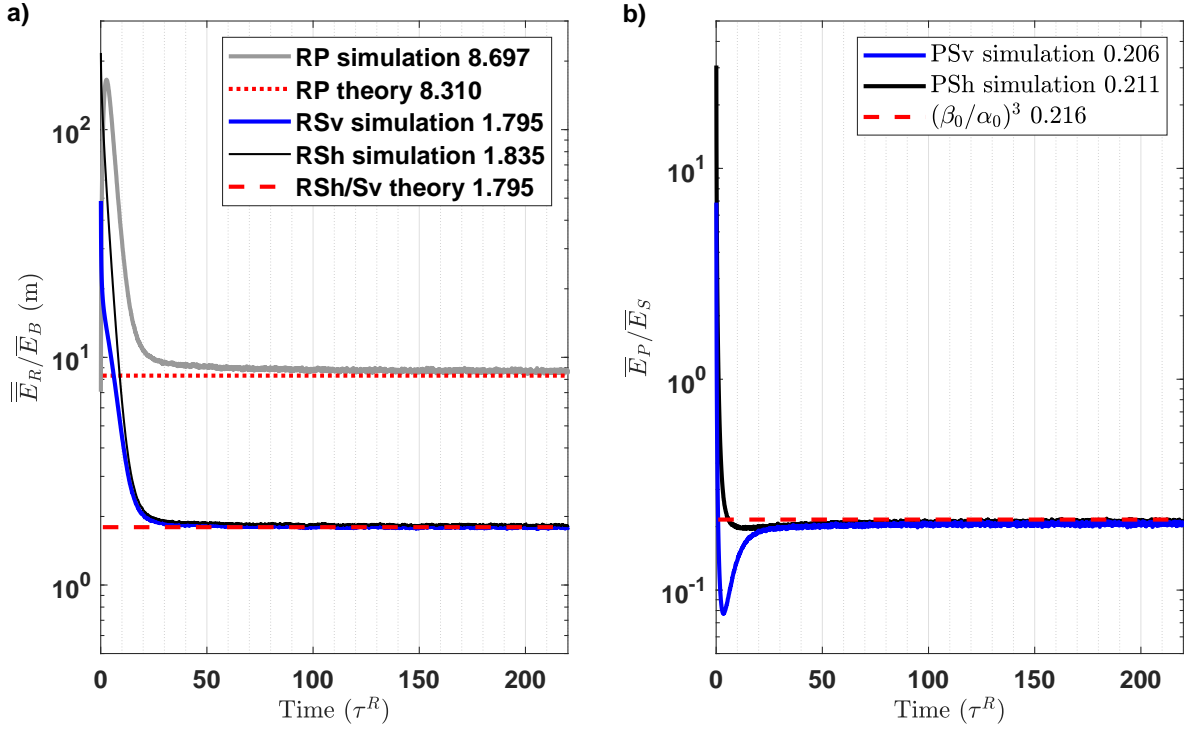


**Figure 3.** Temporal evolution of the energy partitioning ratios among Rayleigh, P, and Sv/h waves in the simulation with the mirror FSBC. We estimate  $\bar{E}_B$  in the shallowest 1 km depth of the medium. We calculate the simulated energy ratio from the last 50  $\tau^R$  simulation results. The theoretical energy ratios are from Equations 17, 18 and 19. We plot the ratios from the simulation results and the equipartition theory in solid and dashed lines, respectively.

## 394 5 DISCUSSION

### 395 5.1 Body-wave incident angles

396 We average the incident-angle-dependent cross sections by assuming that the incident body  
 397 waves are isotropic, i.e. evenly distributed on a unit sphere. We examine this assumption  
 398 here using our simulation results. We discuss the scattering colatitudes ( $\psi_1$  in Figure 1)  
 399 because we actually use the colatitudes in simulation of the wave propagation (e.g.  $\cos(\psi_1)$ ).  
 400 If the scattered-body-wave colatitudes are isotropic,  $\cos(\psi_1)$  will be equal to 1 for all incident  
 401 angles and the incident angles will also be isotropic. The positive and negative cosine values  
 402 represent down-going and up-going wave propagation, respectively. We divide the potential  
 403 range for  $\cos(\psi_1)$ , from -1 to 1, into 180 even bins. At each time step in the simulation, we  
 404 count the particle (i.e. wave) numbers for all types of body waves in each bin from the  
 405 free surface to 10 km depth; we then calculate ratios between the particle numbers and  
 406 the mean of the P particle numbers in all the bins. We finally average the ratios in a time

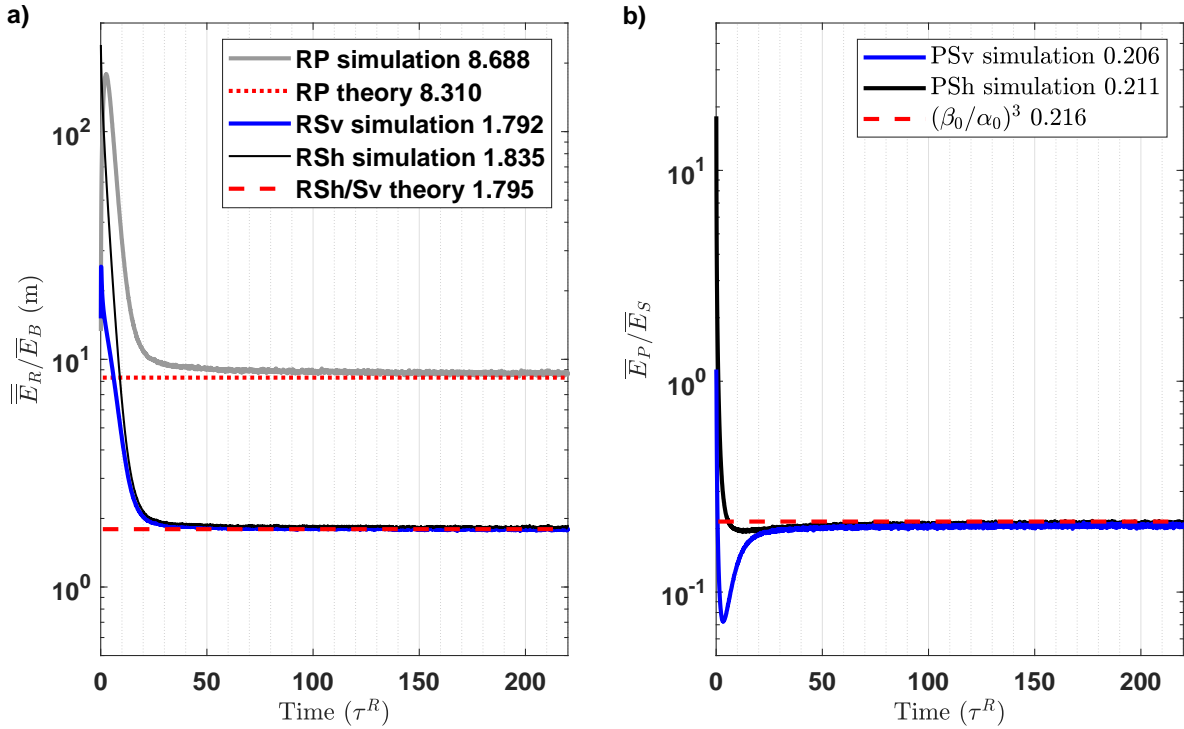


**Figure 4.** Temporal evolution of the energy partitioning ratios among Rayleigh, P and Sv/h waves in the simulation with the mode-conversion FSBC. All data processing and figure settings match those in Figures 3.

407 range when the energy partitioning ratios are stable, such as the last 50 Rayleigh-wave mean  
 408 free times ( $50 \tau^R$ ). We refer to these averaged ratios with respect to  $\cos(\psi_1)$  as angular  
 409 distributions for each type of wave (Figure 5). Based on the isotropic angular distributions,  
 410 we expect the P- and Sv-/Sh-wave ratios to be 1 and  $(\alpha_0/\beta_0)^3$ , respectively. In the two  
 411 FSBC simulation results, we observe similar angular distributions (Figure 5). The P-wave

**Table 1.** Misfits in the simulation results. We calculate the absolute difference between the simulated and theoretical energy equipartition values (Figure 3, 4 and 6), and the misfit value is the ratio of the absolute difference relative to the theoretical energy equipartition value. Simulations with the mirror and mode-conversion FSBCs are presented in Section 4. The simulation with isotropic RB scattering is presented in Section 5.1.

Simulation	RP	RSv	RSh	PSv	PSh
Mirror FSBC	4.7%	0	2.2%	4.6%	2.3%
Mode-conversion FSBC	4.6%	0.2%	2.2%	4.6%	2.3%
Isotropic RB	1.1%	0.3%	0.3%	0.9%	0.9%

distributions are almost isotropic with about 10% off than the expectation, 1, near  $\cos(\psi_1) = 0$  (i.e. parallel to the free surface, the insets in Figure 5a and b). The Sv-wave ratios are slightly elevated from  $\cos(\psi_1) = -1$  to  $\cos(\psi_1) = 0$  (i.e. up-going waves); for the down-going waves, the Sv-wave ratios are perturbed from the expected values with 10% as a maximum near  $\cos(\psi_1) = 0.05$ . The Sh-wave distributions are almost isotropic for all the cosine values and match the theoretical value,  $(\alpha_0/\beta_0)^3$ .

To investigate reasons for the biases in the angular distributions, we propose two tests. First, we check the body-wave angular distributions when we only have body-wave scattering in the simulation. To do that, we turn off the coupling between body and Rayleigh waves, i.e. no RB or BR scattering. We then run this modified simulation with the mode-conversion FSBC and calculate the angular distributions as above. We observe that all the body-wave angular distributions are isotropic after the simulation reaches equipartition (Figure 5c). This observation fits the generalized diffusion theory for the mode-conversion FSBC (e.g. Trégourès & van Tiggelen 2002) and indicates that the biases are not related to body-wave multiple scattering. Second, we turn on the Rayleigh-wave coupling and require the RP and RSv scattering colatitudes to be isotropic while the RSh scattering is already isotropic from the physics (Figure 5d). We observe that this new simulation also generates isotropic distributions for all body waves. Furthermore, this new simulation provides more accurate energy equipartition ratios than the two in Section 4 (Figure 6 and Table 1). Thus, we conclude that the biases in the body-wave angular distributions in the simulation algorithm are due to the anisotropic RP and RSv scattering colatitude patterns. The isotropic scattering patterns can be used in the multiple scattering simulations as done before (e.g. Sato & Nishino 2002). However, the anisotropic RP and RSv scattering patterns are from the physics and change with depth (Figure E1). Therefore this observation and these biases need to be further investigated and more fully understood. This is a new observation that has not been noted in the literature before.

## 5.2 Potential improvements on the simulation

The Monte Carlo simulation algorithm presented here can model body/Rayleigh-wave energy propagating and scattering with a flat free surface, but we cannot model other seismic wave phenomena, such as inhomogeneous waves or nongeometric waves. Inhomogeneous waves are due to shallow seismic sources or seismic wave reflections (e.g. Aki & Richards 2002). Inhomogeneous wave reflection at the free surface can generate nongeometric waves (e.g. Hron & Mikhailenko 1981; Roth & Holliger 2000). We can model these wave phenomena using wave

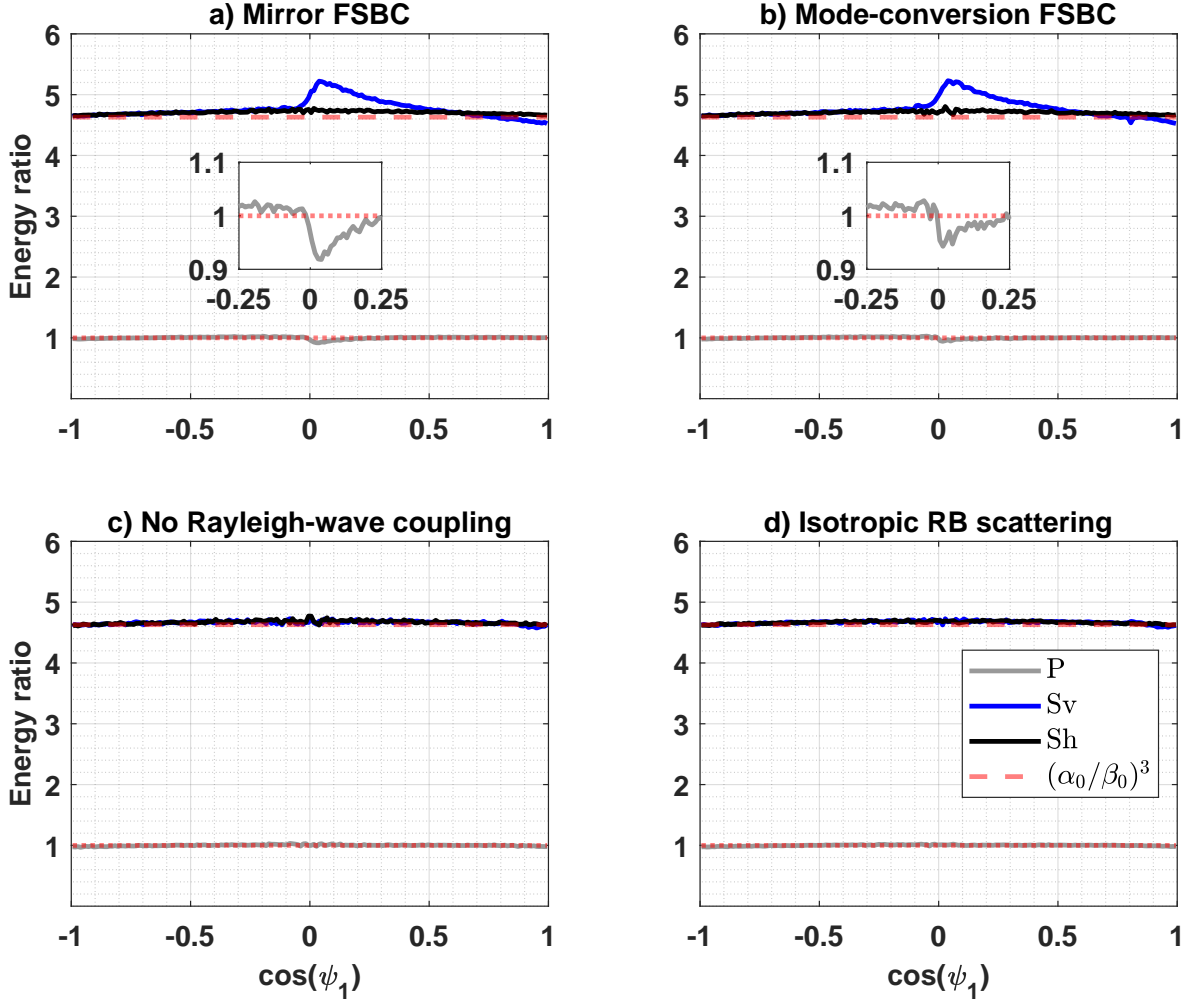


**Figure 5.** The body-wave angular distributions from the simulation with the mirror FSBC (a), the mode-conversion FSBC (b), the mode-conversion FSBC and no RB or BR scattering (c), and the mode-conversion FSBC and isotropic RB scattering (d). We use anisotropic RB scattering in (a) and (b). The theoretical values for the P and Sh/Sv wave are always 1 and  $(\alpha/\beta)^3$  for all  $\cos(\psi_1)$ , respectively. We plot the distributions from the simulation results and the diffusive theory in solid and dashed lines, respectively. The insets in (a) and (b) show zooms of the P-wave distributions at  $\cos(\psi_1) = 0$ .

445 equations, but we have not incorporated these wave phenomena into the radiative transfer  
 446 theory or Monte Carlo simulations yet. We do not consider complex subsurface media such  
 447 as lateral heterogeneities (e.g. Yu et al. 2021), interfaces (e.g. Margerin et al. 1998; Sanborn  
 448 et al. 2017), a topographic free surface (e.g. Snieder 1986b; Takemura et al. 2015; Wang et al.  
 449 2015) or intrinsic attenuation (e.g. Zhang et al. 2021) into our simulations yet. Incorporating  
 450 those into our algorithm is a promising direction for future studies and thus help studies like  
 451 surface waves in microseisms (e.g. Ziane & Hadziioannou 2019; Gualtieri et al. 2020)

452 We model Sv and Sh waves separately in our algorithm. However, in practice, S waves are

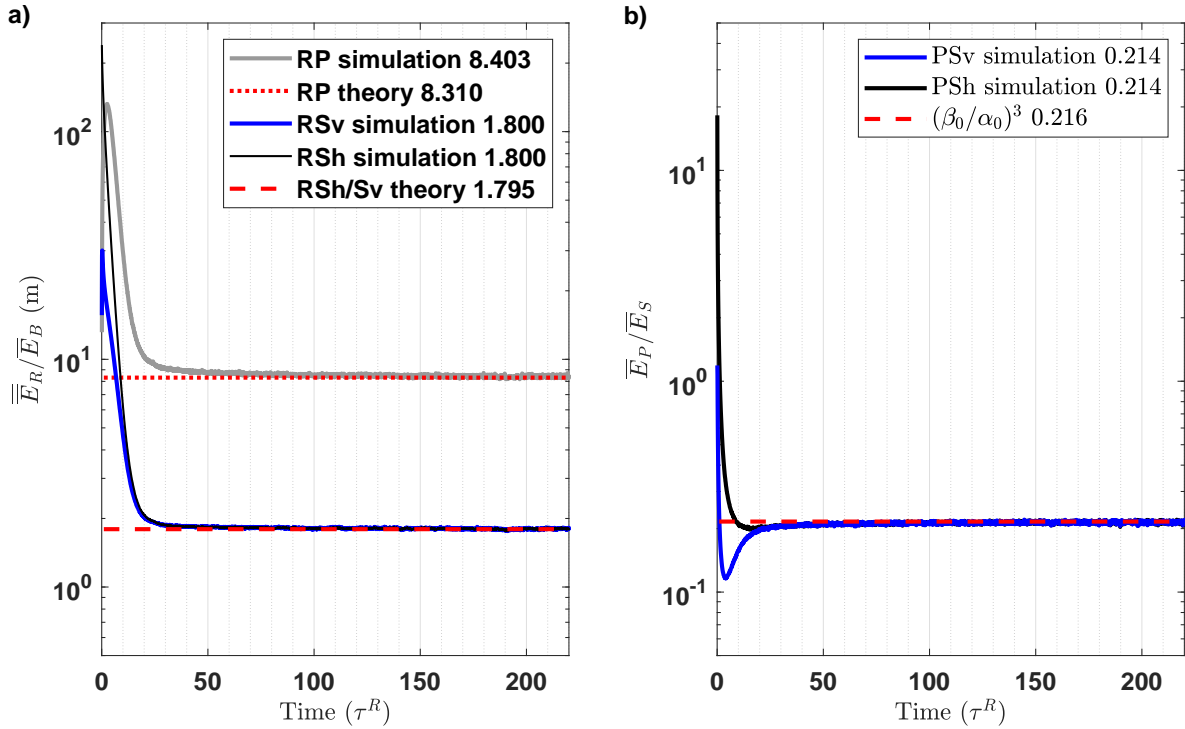


**Figure 6.** Temporal evolution of the energy partitioning ratios among Rayleigh, P and Sv/h waves in the simulation with the mode-conversion FSBC and isotropic RB scattering. All data processing and figure settings match those in Figure 3.

453 commonly combinations of both. One can use the Stokes vector to model the combinations  
 454 in elastic media (e.g. Turner & Weaver 1995; Margerin et al. 2000). In using that approach,  
 455 one needs to track not only the body-wave propagation direction as in our algorithm, but also  
 456 polarization directions. Research regarding incorporation of Rayleigh waves into the Stokes  
 457 vector is still absent and will be helpful for modelling Rayleigh- and Love-wave multiple  
 458 scattering due to different polarization S waves.

## 459 6 CONCLUSION

460 We develop a Monte Carlo simulation algorithm to model body- and surface-wave multiple  
 461 scattering in elastic media. We consider all the possible scattering combinations among P,  
 462 Sv, Sh and Rayleigh waves, and derive the corresponding cross sections due to perturbations  
 463 in elastic properties (i.e. density, Lamé parameter and shear modulus). We use these cross  
 464 sections in the simulation and thus physically incorporate the interaction between body and  
 465 Rayleigh waves during scattering. The algorithm provides the spatio-temporal evolution of  
 466 body- and Rayleigh-wave energies. We focus on density perturbations as scatterers and vali-

467 date the algorithm by comparing the simulation results to the theoretical energy ratios. We  
468 numerically demonstrate that the simulations with the mirror and mode-conversion free sur-  
469 face boundary conditions provide similar energy equipartition ratios close to the theoretical  
470 equipartition values. In the equipartition state, the body-wave angular distributions on the  
471 free surface match Lambert’s cosine law under the two different free surface boundary condi-  
472 tions. Our results also indicate that biases in the simulation results are due to the anisotropic  
473 BR scattering angle patterns. Our research provides a new tool to study the multiple scatter-  
474 ing phenomena in elastic media, and thus may aid coda wave studies such as Q estimation or  
475 interpretation of coda-wave monitoring results.

## 476 **7 ACKNOWLEDGEMENT**

477 The authors thank Grégoire Heller for providing benchmark simulation results. The authors  
478 also thank editor Dr. Christoph Sens-Schönfelder and two anonymous reviewers for their  
479 constructive feedback that helped improve this manuscript. ZX acknowledges support from  
480 the ANR MAGIS (ANR-19-CE31-0008-08). This research is supported by the National Science  
481 Foundation under Grant No. 1643795. We acknowledge high-performance computing support  
482 of the R2 compute cluster (DOI: 10.18122/B2S41H) provided by Boise State University’s  
483 Research Computing.

## 484 **8 DATA AVAILABILITY**

485 The data underlying this article are available in the article.

## 486 **REFERENCES**

- 487 Aki, K., 1992. Scattering conversions P to S versus S to P, *Bulletin of the Seismological Society of*  
488 *America*, **82**(4), 1969–1972.
- 489 Aki, K. & Chouet, B., 1975. Origin of coda waves: source, attenuation, and scattering effects, *Journal*  
490 *of geophysical research*, **80**(23), 3322–3342.
- 491 Aki, K. & Richards, P. G., 2002. *Quantitative Seismology*, Science Books.
- 492 Borcea, L., Garnier, J., & Sølna, K., 2021. Onset of energy equipartition among surface and body  
493 waves, *Proceedings of the Royal Society A*, **477**(2246), 20200775.
- 494 Brenguier, F., Shapiro, N. M., Campillo, M., Nercessian, A., & Ferrazzini, V., 2007. 3-D surface  
495 wave tomography of the Piton de la Fournaise volcano using seismic noise correlations, *Geophysical*  
496 *research letters*, **34**(2).

- 497 Brenguier, F., Shapiro, N. M., Campillo, M., Ferrazzini, V., Duputel, Z., Coutant, O., & Nercessian,  
498 A., 2008. Towards forecasting volcanic eruptions using seismic noise, *Nature Geoscience*, **1**(2), 126.
- 499 Clements, T. & Denolle, M. A., 2018. Tracking groundwater levels using the ambient seismic field,  
500 *Geophysical Research Letters*, **45**(13), 6459–6465.
- 501 Grêt, A., Snieder, R., Aster, R. C., & Kyle, P. R., 2005. Monitoring rapid temporal change in a  
502 volcano with coda wave interferometry, *Geophysical Research Letters*, **32**(6).
- 503 Gualtieri, L., Bachmann, E., Simons, F. J., & Tromp, J., 2020. The origin of secondary microseism  
504 love waves, *Proceedings of the National Academy of Sciences*, **117**(47), 29504–29511.
- 505 Gusev, A. & Abubakirov, I., 1987. Monte-Carlo simulation of record envelope of a near earthquake,  
506 *Physics of the Earth and Planetary Interiors*, **49**(1-2), 30–36.
- 507 Hoshihara, M., 1991. Simulation of multiple-scattered coda wave excitation based on the energy con-  
508 servation law, *Physics of the Earth and Planetary Interiors*, **67**(1-2), 123–136.
- 509 Hoshihara, M., 1995. Estimation of nonisotropic scattering in western Japan using coda wave envelopes:  
510 Application of a multiple nonisotropic scattering model, *Journal of Geophysical Research: Solid  
511 Earth*, **100**(B1), 645–657.
- 512 Hoshihara, M., 1997. Seismic coda wave envelope in depth-dependent S wave velocity structure, *Physics  
513 of the Earth and Planetary Interiors*, **104**(1-3), 15–22.
- 514 Hron, F. & Mikhaïlenko, B., 1981. Numerical modeling of nongeometrical effects by the Alekseev-  
515 Mikhaïlenko method, *Bulletin of the Seismological Society of America*, **71**(4), 1011–1029.
- 516 Lagendijk, A. & Van Tiggelen, B. A., 1996. Resonant multiple scattering of light, *Physics Reports*,  
517 **270**(3), 143–215.
- 518 Larose, E., Planes, T., Rossetto, V., & Margerin, L., 2010. Locating a small change in a multiple  
519 scattering environment, *Applied Physics Letters*, **96**(20), 204101.
- 520 Lux, I. & Koblinger, L., 1991. *Monte Carlo particle transport methods: neutron and photon calcula-  
521 tions*, CRC Press.
- 522 Maeda, T., Sato, H., & Nishimura, T., 2008. Synthesis of coda wave envelopes in randomly inhom-  
523 geneous elastic media in a half-space: single scattering model including rayleigh waves, *Geophysical  
524 Journal International*, **172**(1), 130–154.
- 525 Mainsant, G., Larose, E., Brönnimann, C., Jongmans, D., Michoud, C., & Jaboyedoff, M., 2012. Am-  
526 bient seismic noise monitoring of a clay landslide: Toward failure prediction, *Journal of Geophysical  
527 Research: Earth Surface*, **117**(F1).
- 528 Margerin, L., 2009. Generalized eigenfunctions of layered elastic media and application to diffuse  
529 fields, *The Journal of the Acoustical Society of America*, **125**(1), 164–174.
- 530 Margerin, L., Campillo, M., & Tiggelen, B., 1998. Radiative transfer and diffusion of waves in a  
531 layered medium: new insight into coda Q, *Geophysical journal international*, **134**(2), 596–612.
- 532 Margerin, L., Campillo, M., Shapiro, N., & van Tiggelen, B., 1999. Residence time of diffuse waves  
533 in the crust as a physical interpretation of coda Q: application to seismograms recorded in Mexico,

- 534 *Geophysical Journal International*, **138**(2), 343–352.
- 535 Margerin, L., Campillo, M., & Van Tiggelen, B., 2000. Monte Carlo simulation of multiple scattering  
536 of elastic waves, *Journal of Geophysical Research: Solid Earth*, **105**(B4), 7873–7892.
- 537 Margerin, L., Planès, T., Mayor, J., & Calvet, M., 2016. Sensitivity kernels for coda-wave interferom-  
538 etry and scattering tomography: theory and numerical evaluation in two-dimensional anisotropically  
539 scattering media, *Geophysical Journal International*, **204**(1), 650–666.
- 540 Margerin, L., Bajasas, A., & Campillo, M., 2019. A scalar radiative transfer model including the  
541 coupling between surface and body waves, *Geophysical Journal International*, **219**(2), 1092–1108.
- 542 Mikesell, T. D., Malcolm, A. E., Yang, D., & Haney, M. M., 2015. A comparison of methods to  
543 estimate seismic phase delays: Numerical examples for coda wave interferometry, *Geophysical Journal  
544 International*, **202**(1), 347–360.
- 545 Mordret, A., Mikesell, T. D., Harig, C., Lipovsky, B. P., & Prieto, G. A., 2016. Monitoring southwest  
546 Greenland’s ice sheet melt with ambient seismic noise, *Science advances*, **2**(5), e1501538.
- 547 Obermann, A., Planès, T., Larose, E., Sens-Schönfelder, C., & Campillo, M., 2013. Depth sensitivity  
548 of seismic coda waves to velocity perturbations in an elastic heterogeneous medium, *Geophysical  
549 Journal International*, **194**(1), 372–382.
- 550 Obermann, A., Kraft, T., Larose, E., & Wiemer, S., 2015. Potential of ambient seismic noise techniques  
551 to monitor the St. Gallen geothermal site (Switzerland), *Journal of Geophysical Research: Solid  
552 Earth*, **120**(6), 4301–4316.
- 553 Obermann, A., Planès, T., Hadziioannou, C., & Campillo, M., 2016. Lapse-time-dependent coda-wave  
554 depth sensitivity to local velocity perturbations in 3-D heterogeneous elastic media, *Geophysical  
555 Journal International*, **207**(1), 59–66.
- 556 Obermann, A., Planès, T., Larose, E., & Campillo, M., 2019. 4-D Imaging of Subsurface Changes  
557 with Coda Waves: Numerical Studies of 3-D Combined Sensitivity Kernels and Applications to the  
558  $M_w$ 7.9, 2008 Wenchuan Earthquake, *Pure and Applied Geophysics*, **176**(3), 1243–1254.
- 559 Pacheco, C. & Snieder, R., 2005. Time-lapse travel time change of multiply scattered acoustic waves,  
560 *The Journal of the Acoustical Society of America*, **118**(3), 1300–1310.
- 561 Paul, A., Campillo, M., Margerin, L., Larose, E., & Derode, A., 2005. Empirical synthesis of time-  
562 asymmetrical Green functions from the correlation of coda waves, *Journal of Geophysical Research:  
563 Solid Earth*, **110**(B8).
- 564 Planès, T., Larose, E., Rossetto, V., & Margerin, L., 2015. Imaging multiple local changes in het-  
565 erogeneous media with diffuse waves, *The Journal of the Acoustical Society of America*, **137**(2),  
566 660–667.
- 567 Poupinet, G., Ellsworth, W., & Frechet, J., 1984. Monitoring velocity variations in the crust using  
568 earthquake doublets: An application to the Calaveras Fault, California, *Journal of Geophysical  
569 Research: Solid Earth*, **89**(B7), 5719–5731.
- 570 Roth, M. & Holliger, K., 2000. The non-geometric P S wave in high-resolution seismic data: obser-

- 571 variations and modelling, *Geophysical Journal International*, **140**(1), F5–F11.
- 572 Ryzhik, L., Papanicolaou, G., & Keller, J. B., 1996. Transport equations for elastic and other waves  
573 in random media, *Wave motion*, **24**(4), 327–370.
- 574 Sanborn, C. J., Cormier, V. F., & Fitzpatrick, M., 2017. Combined effects of deterministic and  
575 statistical structure on high-frequency regional seismograms, *Geophysical Journal International*,  
576 **210**(2), 1143–1159.
- 577 Sato, H., 1994. Multiple isotropic scattering model including PS conversions for the seismogram  
578 envelope formation, *Geophysical Journal International*, **117**(2), 487–494.
- 579 Sato, H. & Nishino, M., 2002. Multiple isotropic-scattering model on the spherical earth for the  
580 synthesis of rayleigh-wave envelopes, *Journal of Geophysical Research: Solid Earth*, **107**(B12), ESE–  
581 7.
- 582 Sécher, P., 1998. Étude spectrale du système différentiel  $2 \times 2$  associé à un problème d'élasticité linéaire,  
583 *Annales de la Faculté des sciences de Toulouse : Mathématiques*, **7**(4), 699–726.
- 584 Sens-Schönfelder, C. & Wegler, U., 2006. Passive image interferometry and seasonal variations of  
585 seismic velocities at Merapi Volcano, Indonesia, *Geophysical research letters*, **33**(21).
- 586 Shapiro, N., Campillo, M., Margerin, L., Singh, S., Kostoglodov, V., & Pacheco, J., 2000. The energy  
587 partitioning and the diffusive character of the seismic coda, *Bulletin of the Seismological Society of*  
588 *America*, **90**(3), 655–665.
- 589 Snieder, R., 1986a. 3-d linearized scattering of surface waves and a formalism for surface wave  
590 holography, *Geophysical Journal International*, **84**(3), 581–605.
- 591 Snieder, R., 1986b. The influence of topography on the propagation and scattering of surface waves,  
592 *Physics of the earth and planetary interiors*, **44**(3), 226–241.
- 593 Snieder, R., 2006. The theory of coda wave interferometry, *Pure and Applied geophysics*, **163**(2-3),  
594 455–473.
- 595 Snieder, R., Grêt, A., Douma, H., & Scales, J., 2002. Coda wave interferometry for estimating  
596 nonlinear behavior in seismic velocity, *Science*, **295**(5563), 2253–2255.
- 597 Takemura, S., Furumura, T., & Maeda, T., 2015. Scattering of high-frequency seismic waves caused  
598 by irregular surface topography and small-scale velocity inhomogeneity, *Geophysical Journal Inter-*  
599 *national*, **201**(1), 459–474.
- 600 Trégourès, N. P. & van Tiggelen, B. A., 2002. Generalized diffusion equation for multiple scattered  
601 elastic waves, *Waves in random media*, **12**, 21–38.
- 602 Tregoures, N. P. & Van Tiggelen, B. A., 2002. Quasi-two-dimensional transfer of elastic waves,  
603 *Physical Review E*, **66**(3), 036601.
- 604 Turner, J. A. & Weaver, R. L., 1995. Time dependence of multiply scattered diffuse ultrasound in  
605 polycrystalline media, *The Journal of the Acoustical Society of America*, **97**(5), 2639–2644.
- 606 Wang, L., Xu, Y., & Luo, Y., 2015. Numerical Investigation of 3D multichannel analysis of surface  
607 wave method, *Journal of Applied Geophysics*, **119**, 156–169.

- 608 Wang, Q. Y., Brenguier, F., Campillo, M., Lecointre, A., Takeda, T., & Aoki, 2017. Seasonal crustal  
609 seismic velocity changes throughout Japan, *Journal of Geophysical Research: Solid Earth*, **122**(10),  
610 7987–8002.
- 611 Weaver, R. L., 1982. On diffuse waves in solid media, *The Journal of the Acoustical Society of*  
612 *America*, **71**(6), 1608–1609.
- 613 Weaver, R. L., 1990. Diffusivity of ultrasound in polycrystals, *Journal of the Mechanics and Physics*  
614 *of Solids*, **38**(1), 55–86.
- 615 Wu, R.-S., 1985. Multiple scattering and energy transfer of seismic waves—separation of scattering  
616 effect from intrinsic attenuation—i. theoretical modelling, *Geophysical Journal International*, **82**(1),  
617 57–80.
- 618 Wu, R.-S. & Aki, K., 1985. Scattering characteristics of elastic waves by an elastic heterogeneity,  
619 *Geophysics*, **50**(4), 582–595.
- 620 Yu, C., Castellanos, J. C., & Zhan, Z., 2021. Imaging strong lateral heterogeneities across the con-  
621 tiguous US using body-to-surface wave scattering, *Journal of Geophysical Research. Solid Earth*,  
622 **126**(1), Art–No.
- 623 Zeng, Y., 1993. Theory of scattered P-and S-wave energy in a random isotropic scattering medium,  
624 *Bulletin of the Seismological Society of America*, **83**(4), 1264–1276.
- 625 Zeng, Y., 2006. Scattered surface wave energy in the seismic coda, *Pure and Applied Geophysics*,  
626 **163**(2-3), 533–548.
- 627 Zhang, T., Sens-Schönfelder, C., & Margerin, L., 2021. Sensitivity kernels for static and dynamic  
628 tomography of scattering and absorbing media with elastic waves: a probabilistic approach, *Geo-*  
629 *physical Journal International*, **225**(3), 1824–1853.
- 630 Ziane, D. & Hadziioannou, C., 2019. The contribution of multiple scattering to love wave generation  
631 in the secondary microseism, *Geophysical Journal International*, **217**(2), 1108–1122.

## 632 APPENDIX A: RAYLEIGH WAVE EIGENFUNCTIONS

Rayleigh waves possess displacements in the vertical (Z) and radial (R) directions. In a 1D elastic medium, one can write the two component displacement at frequency  $\omega$  and depth  $z$  as

$$u_R = r_1(z, \omega) \exp[i(k_R \Delta - \omega t)], \quad (\text{A.1})$$

$$u_Z = r_2(z, \omega) \exp[i(k_R \Delta - \omega t)], \quad (\text{A.2})$$

633 where  $r_1$  and  $r_2$  are the eigenfunctions,  $k_R$  is the Rayleigh-wave wavenumber, and  $\Delta$  is the  
634 propagation distance (Aki & Richards 2002, Chapter 7.2). One calculates the two eigenfunc-  
635 tions based on boundary conditions: vanishing traction at the free surface and zero displace-  
636 ment at infinity (e.g. Aki & Richards 2002, Chapter 7.2.1). In a homogeneous halfspace, the

analytical expressions for the eigenfunctions are

$$r_1(z, \omega) = -k_R \exp(-k_R \sqrt{1 - \frac{c_R^2}{\alpha_0^2}} z) + k_R \frac{2\beta_0^2 - c_R^2}{2\beta_0^2} \exp(-k_R \sqrt{1 - \frac{c_R^2}{\beta_0^2}} z), \quad (\text{A.3})$$

and

$$r_2(z, \omega) = -k_R \sqrt{1 - \frac{c_R^2}{\alpha_0^2}} \exp(-k_R \sqrt{1 - \frac{c_R^2}{\alpha_0^2}} z) + k_R \frac{2\sqrt{1 - \frac{c_R^2}{\alpha_0^2}}}{2 - \frac{c_R^2}{\beta_0^2}} \exp(-k_R \sqrt{1 - \frac{c_R^2}{\beta_0^2}} z). \quad (\text{A.4})$$

We calculate the eigenfunctions for the velocity model where  $\alpha_0=5$  km/s and  $\beta_0=3$  km/s (Figure A1), and we use the eigenfunctions in the scattering amplitudes (e.g. Equation 7) and cross sections (e.g. Equation 10).

## APPENDIX B: SCATTERING CROSS SECTIONS

### B1 Body-to-Rayleigh-wave cross sections

For scattering due to perturbations in the Lamé parameter (i.e.  $\delta\lambda$ ),

$$\sigma_\lambda^{PR} = \frac{k_P^3 (\alpha_0^2 - 2\beta_0^2)^2}{4c_R U_R^3 \int (r_1^2 + r_2^2) dz} \left( r_1 + \frac{1}{k_R} \frac{\partial r_2}{\partial z} \right)^2 V^2 \left( \frac{\delta\lambda}{\lambda_0} \right)^2, \quad (\text{B.1})$$

$$\sigma_\lambda^{SvR} = \sigma_\lambda^{ShR} = 0. \quad (\text{B.2})$$

For  $\delta\rho$  scatters,

$$\sigma_\rho^{PR} = \frac{\omega^3}{8\alpha_0 c_R U_R \int (r_1^2 + r_2^2) dz} [r_1^2 \sin^2(\psi_0) + 2r_2^2 \cos^2(\psi_0)] V^2 \left( \frac{\delta\rho}{\rho_0} \right)^2, \quad (\text{B.3})$$

$$\sigma_\rho^{SvR} = \frac{\omega^3}{8\beta_0 c_R U_R \int (r_1^2 + r_2^2) dz} [r_1^2 \cos^2(\psi_0) + 2r_2^2 \sin^2(\psi_0)] V^2 \left( \frac{\delta\rho}{\rho_0} \right)^2, \quad (\text{B.4})$$

$$\sigma_\rho^{ShR} = \frac{\omega^3}{8\beta_0 c_R U_R \int (r_1^2 + r_2^2) dz} r_1^2 V^2 \left( \frac{\delta\rho}{\rho_0} \right)^2, \quad (\text{B.5})$$

where  $\psi_0$  is the body-wave incident angle (Figure 1). After averaging over incident angles,

$$\tilde{\sigma}_\rho^{PR} = \frac{1}{\int_0^\pi \sin(\psi_0) d\psi_0} \int_0^\pi \sigma_\rho^{PR} \sin(\psi_0) d\psi_0 = \frac{\omega^3}{12\alpha_0 c_R U_R \int (r_1^2 + r_2^2) dz} (r_1^2 + r_2^2) V^2 \left( \frac{\delta\rho}{\rho_0} \right)^2, \quad (\text{B.6})$$

$$\tilde{\sigma}_\rho^{SvR} = \frac{1}{\int_0^\pi \sin(\psi_0) d\psi_0} \int_0^\pi \sigma_\rho^{SvR} \sin(\psi_0) d\psi_0 = \frac{\omega^3}{24\beta_0 c_R U_R \int (r_1^2 + r_2^2) dz} (r_1^2 + 4r_2^2) V^2 \left( \frac{\delta\rho}{\rho_0} \right)^2, \quad (\text{B.7})$$

$$\tilde{\sigma}_\rho^{ShR} = \sigma_\rho^{ShR}. \quad (\text{B.8})$$

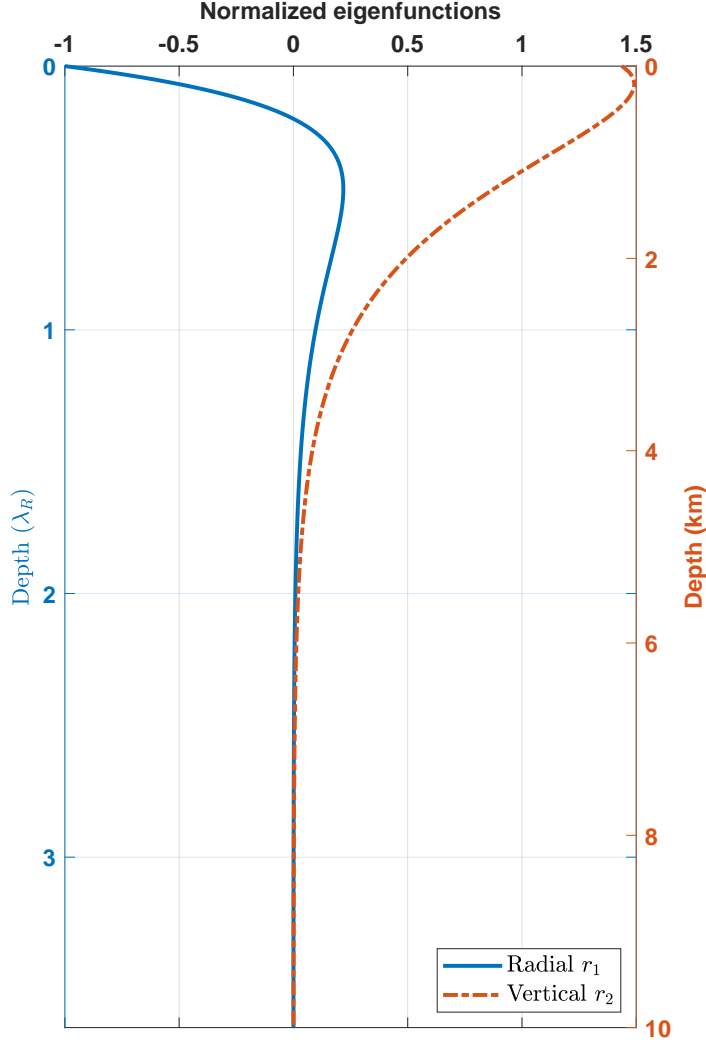


**Figure A1.** Radial ( $r_1$ ) and vertical ( $r_2$ ) eigenfunctions vary with depth at 1 Hz. The eigenfunction values are normalized by the absolute value of  $r_1$  at the free surface ( $z = 0$ ). The depth axes are Rayleigh-wave wavelength ( $\lambda_R$ ) and kilometers to demonstrate how shallow scatterers must be in order to generate Rayleigh waves.

647

For perturbations in shear modulus ( $\delta\mu$ ),

$$\sigma_\mu^{PR} = \frac{\omega^3 \beta_0^4}{8\alpha_0^3 c_R U_R^3 \int (r_1^2 + r_2^2) dz} \left[ 3r_1^2 \sin^4(\psi_0) + \frac{8}{k_R^2} \left( \frac{\partial r_2}{\partial z} \right)^2 \cos^4(\psi_0) + \frac{8r_1}{k_R} \frac{\partial r_2}{\partial z} \sin^2(\psi_0) \cos^2(\psi_0) \right. \\ \left. + \frac{1}{k_R^2} \left( \frac{\partial r_1}{\partial z} \right)^2 \sin^2(2\psi_0) + r_2^2 \sin^2(2\psi_0) - \frac{2}{k_R} \frac{\partial r_1}{\partial z} r_2 \sin^2(2\psi_0) \right] V^2 \left( \frac{\delta\mu}{\mu_0} \right)^2, \quad (\text{B.9})$$

$$\sigma_\mu^{SvR} = \frac{\omega^3 \beta_0}{8c_R U_R^3 \int (r_1^2 + r_2^2) dz} \left[ \frac{3}{4} r_1^2 \sin^2(2\psi_0) + \frac{2}{k_R^2} \left( \frac{\partial r_2}{\partial z} \right)^2 \sin^2(2\psi_0) - \frac{2}{k_R} r_1 \frac{\partial r_2}{\partial z} \sin^2(2\psi_0) \right. \\ \left. + r_2^2 \cos^2(2\psi_0) + \frac{1}{k_R^2} \left( \frac{\partial r_1}{\partial z} \right)^2 \cos^2(2\psi_0) - \frac{2}{k_R} \frac{\partial r_1}{\partial z} r_2 \cos^2(2\psi_0) \right] V^2 \left( \frac{\delta\mu}{\mu_0} \right)^2, \quad (\text{B.10})$$

$$\sigma_\mu^{ShR} = \frac{\omega^3 \beta_0}{8c_R U_R^3 \int (r_1^2 + r_2^2) dz} \left[ r_1^2 \sin^2(\psi_0) + r_2^2 \cos^2(\psi_0) + \frac{1}{k_R^2} \left( \frac{\partial r_1}{\partial z} \right)^2 - \frac{2}{k_R} \frac{\partial r_1}{\partial z} r_2 \cos(\psi_0) \right] V^2 \left( \frac{\delta\mu}{\mu_0} \right)^2. \quad (\text{B.11})$$

648 After averaging over incident angles,

$$\tilde{\sigma}_\mu^{PR} = \frac{\omega^3 \beta_0^4}{15\alpha_0^3 c_R U_R^3 \int (r_1^2 + r_2^2) dz} \left[ 3r_1^2 + \frac{3}{k_R^2} \left( \frac{\partial r_2}{\partial z} \right)^2 + \frac{2r_1}{k_R} \frac{\partial r_2}{\partial z} + \frac{1}{k_R^2} \left( \frac{\partial r_1}{\partial z} \right)^2 + r_2^2 - \frac{2}{k_R} \frac{\partial r_1}{\partial z} r_2 \right] V^2 \left( \frac{\delta\mu}{\mu_0} \right)^2, \quad (\text{B.12})$$

$$\tilde{\sigma}_\mu^{SvR} = \frac{\omega^3 \beta_0}{c_R U_R^3 \int (r_1^2 + r_2^2) dz} \left[ \frac{r_1^2}{20} + \frac{2}{15k_R^2} \left( \frac{\partial r_2}{\partial z} \right)^2 - \frac{2}{15k_R} r_1 \frac{\partial r_2}{\partial z} + \frac{7}{120} r_2^2 + \frac{7}{120k_R^2} \left( \frac{\partial r_1}{\partial z} \right)^2 - \frac{7}{60k_R} \frac{\partial r_1}{\partial z} r_2 \right] V^2 \left( \frac{\delta\mu}{\mu_0} \right)^2, \quad (\text{B.13})$$

$$\tilde{\sigma}_\mu^{ShR} = \frac{\omega^3 \beta_0}{16c_R U_R^3 \int (r_1^2 + r_2^2) dz} \left[ \frac{4}{3} r_1^2 + \frac{2}{3} r_2^2 + \frac{2}{k_R^2} \left( \frac{\partial r_1}{\partial z} \right)^2 \right] V^2 \left( \frac{\delta\mu}{\mu_0} \right)^2. \quad (\text{B.14})$$

## 649 B2 Rayleigh-to-body-wave cross sections

650 For perturbations in the Lamé parameter ( $\delta\lambda$ ),

$$\bar{\sigma}_\lambda^{RP} = \frac{k_P^4 (\alpha_0^2 - 2\beta_0^2)^2}{4\pi\alpha_0 c_R^2 U_R \int (r_1^2 + r_2^2) dz} \int \left( r_1 + \frac{1}{k_R} \frac{\partial r_2}{\partial z} \right)^2 dz_s V^2 \left( \frac{\delta\lambda}{\lambda_0} \right)^2, \quad (\text{B.15})$$

$$\sigma_\lambda^{RSv} = \sigma_\lambda^{RSh} = 0, \quad (\text{B.16})$$

651 where  $\bar{\sigma}$  is the integral of  $\sigma$  over depth (e.g. Equation 12).

652 For perturbations in density ( $\delta\rho$ ),

$$\bar{\sigma}_\rho^{RP} = \frac{\omega k_P^3}{12\pi U_R} V^2 \left( \frac{\delta\rho}{\delta\rho_0} \right)^2, \quad (\text{B.17})$$

$$\bar{\sigma}_\rho^{RSv} = \frac{\omega k_S^3}{24\pi U_R} \frac{\int (r_1^2 + 4r_2^2) dz_s}{\int (r_1^2 + r_2^2) dz} V^2 \left( \frac{\delta\rho}{\delta\rho_0} \right)^2, \quad (\text{B.18})$$

$$\bar{\sigma}_\rho^{RSh} = \frac{\omega k_S^3}{8\pi U_R} \frac{\int r_1^2 dz_s}{\int (r_1^2 + r_2^2) dz} V^2 \left( \frac{\delta\rho}{\delta\rho_0} \right)^2. \quad (\text{B.19})$$

653 For perturbations in shear modulus ( $\delta\mu$ ),

$$\bar{\sigma}_\mu^{RP} = \frac{k_P^4 \beta_0^4}{15\pi\alpha_0 c_R^2 U_R \int (r_1^2 + r_2^2) dz} \int \left[ 3r_1^2 + \frac{3}{k_R^2} \left( \frac{\partial r_2}{\partial z} \right)^2 + 2\frac{r_1}{k_R} \frac{\partial r_2}{\partial z} + \frac{1}{k_R^2} \left( \frac{\partial r_1}{\partial z} \right)^2 + r_2^2 - \frac{2}{k_R} \frac{\partial r_1}{\partial z} r_2 \right] dz_s V^2 \left( \frac{\delta\mu}{\mu_0} \right)^2, \quad (\text{B.20})$$

$$\bar{\sigma}_\mu^{RSv} = \frac{\omega^3 k_S}{\pi c_R^2 U_R \int (r_1^2 + r_2^2) dz} \int \left[ \frac{1}{20} r_1^2 + \frac{2}{15k_R^2} \left( \frac{\partial r_2}{\partial z} \right)^2 - \frac{2}{15k_R} r_1 \frac{\partial r_2}{\partial z} + \frac{7}{120} r_2^2 + \frac{7}{120k_R^2} \left( \frac{\partial r_1}{\partial z} \right)^2 - \frac{7}{60k_R} \frac{\partial r_1}{\partial z} r_2 \right] dz_s V^2 \left( \frac{\delta\mu}{\mu_0} \right)^2, \quad (\text{B.21})$$

$$\bar{\sigma}_\mu^{RSh} = \frac{\omega^3 k_S}{\pi c_R^2 U_R \int (r_1^2 + r_2^2) dz} \int \left[ \frac{r_1^2}{12} + \frac{r_2^2}{24} + \frac{1}{8k_R^2} \left( \frac{\partial r_1}{\partial z} \right)^2 \right] dz_s V^2 \left( \frac{\delta\mu}{\mu_0} \right)^2. \quad (\text{B.22})$$

654 **B3 Rayleigh-to-Rayleigh-wave cross sections**

$$\bar{\sigma}_\lambda^{RR} = \frac{\omega^3(\alpha_0^2 - 2\beta_0^2)^2}{4c_R^5 U_R^2 [\int (r_1^2 + r_2^2) dz]^2} \int \left( r_1 + \frac{1}{k_R} \frac{\partial r_2}{\partial z} \right)^4 dz_s V^2 \left( \frac{\delta\lambda}{\lambda_0} \right)^2, \quad (\text{B.23})$$

$$\bar{\sigma}_\rho^{RR} = \frac{\omega^3}{8c_R U_R^2 [\int (r_1^2 + r_2^2) dz]^2} \int (r_1^4 + 2r_2^4) dz_s V^2 \left( \frac{\delta\rho}{\rho_0} \right)^2, \quad (\text{B.24})$$

$$\bar{\sigma}_\mu^{RR} = \frac{\omega^3 \beta_0^4}{8c_R^5 U_R^2 [\int (r_1^2 + r_2^2) dz]^2} \int \left[ 3r_1^4 + \left( r_2 - \frac{1}{k_R} \frac{\partial r_1}{\partial z} \right)^4 + \frac{8}{k_R^4} \left( \frac{\partial r_2}{\partial z} \right)^4 + \frac{8}{k_R^2} r_1^2 \left( \frac{\partial r_2}{\partial z} \right)^2 \right] dz_s V^2 \left( \frac{\delta\mu}{\mu_0} \right)^2. \quad (\text{B.25})$$

655 **B4 Body-to-body-wave cross sections**656 For perturbations in the Lamé parameter ( $\delta\lambda$ ),

$$\sigma_\lambda^{PP} = \frac{k_P^4}{4\pi} \left( \frac{\alpha_0^2 - 2\beta_0^2}{\alpha_0^2} \right)^2 V^2 \left( \frac{\delta\lambda}{\lambda_0} \right)^2, \quad (\text{B.26})$$

$$\sigma_\lambda^{PSh} = \sigma_\lambda^{PSv} = \sigma_\lambda^{ShP} = \sigma_\lambda^{SvP} = 0. \quad (\text{B.27})$$

657 For perturbations in the density ( $\delta\rho$ ), we write the cross sections

$$\sigma_\rho^{PP} = \frac{k_P^4}{12\pi} V^2 \left( \frac{\delta\rho}{\rho_0} \right)^2, \quad (\text{B.28})$$

$$\sigma_\rho^{PSv} = \frac{\beta_0 k_s^4}{24\pi \alpha_0} [1 + 3 \cos^2(\psi_0)] V^2 \left( \frac{\delta\rho}{\rho_0} \right)^2, \quad (\text{B.29})$$

$$\sigma_\rho^{PSh} = \frac{\beta_0 k_s^4}{8\pi \alpha_0} \sin^2(\psi_0) V^2 \left( \frac{\delta\rho}{\rho_0} \right)^2, \quad (\text{B.30})$$

$$\sigma_\rho^{SvP} = \sigma_\rho^{ShP} = \frac{\alpha_0 k_P^4}{12\pi \beta_0} V^2 \left( \frac{\delta\rho}{\rho_0} \right)^2, \quad (\text{B.31})$$

$$\sigma_\rho^{SvSv} = \frac{k_S^4}{24\pi} [1 + 3 \sin^2(\psi_0)] V^2 \left( \frac{\delta\rho}{\rho_0} \right)^2, \quad (\text{B.32})$$

$$\sigma_\rho^{SvSh} = \frac{k_S^4}{8\pi} \cos^2(\psi_0) V^2 \left( \frac{\delta\rho}{\rho_0} \right)^2, \quad (\text{B.33})$$

$$\sigma_\rho^{ShSv} = \frac{k_S^4}{24\pi} V^2 \left( \frac{\delta\rho}{\rho_0} \right)^2, \quad (\text{B.34})$$

$$\sigma_\rho^{ShSh} = \frac{k_S^4}{8\pi} V^2 \left( \frac{\delta\rho}{\rho_0} \right)^2. \quad (\text{B.35})$$

658 and the averaged cross sections over incident angles

$$\tilde{\sigma}_\rho^{PSv} = \frac{\beta_0 k_s^4}{12\pi\alpha_0} V^2 \left( \frac{\delta\rho}{\rho_0} \right)^2, \quad (\text{B.36})$$

$$\tilde{\sigma}_\rho^{PSh} = \frac{\beta_0 k_s^4}{12\pi\alpha_0} V^2 \left( \frac{\delta\rho}{\rho_0} \right)^2, \quad (\text{B.37})$$

$$\tilde{\sigma}_\rho^{SvSv} = \frac{k_S^4}{8\pi} V^2 \left( \frac{\delta\rho}{\rho_0} \right)^2, \quad (\text{B.38})$$

$$\tilde{\sigma}_\rho^{SvSh} = \frac{k_S^4}{24\pi} V^2 \left( \frac{\delta\rho}{\rho_0} \right)^2. \quad (\text{B.39})$$

659 For perturbations in shear modulus ( $\delta\mu$ ),

$$\sigma_\mu^{PP} = \frac{k_P^4 \beta_0^4}{5\pi\alpha_0^4} V^2 \left( \frac{\delta\mu}{\mu_0} \right)^2, \quad (\text{B.40})$$

$$\sigma_\mu^{PSv} = \frac{\beta_0 k_S^2 k_P^2}{60\pi\alpha_0} [3 + 5 \cos^4(\psi_0)] V^2 \left( \frac{\delta\mu}{\mu_0} \right)^2, \quad (\text{B.41})$$

$$\sigma_\mu^{PSh} = \frac{\beta_0 k_S^2 k_P^2}{12\pi\alpha_0} [\sin^4(\psi_0) + 2 \sin^2(\psi_0) \cos^2(\psi_0)] V^2 \left( \frac{\delta\mu}{\mu_0} \right)^2, \quad (\text{B.42})$$

$$\sigma_\mu^{SvP} = \sigma_\mu^{ShP} = \frac{1}{15} \frac{k_P^4 \beta_0}{\pi\alpha_0} V^2 \left( \frac{\delta\mu}{\mu_0} \right)^2, \quad (\text{B.43})$$

$$\sigma_\mu^{SvSv} = \frac{k_S^4}{120\pi} [38 \sin^2(\psi_0) \cos^2(\psi_0) + 7 \cos^2(2\psi_0)] V^2 \left( \frac{\delta\mu}{\mu_0} \right)^2, \quad (\text{B.44})$$

$$\sigma_\mu^{SvSh} = \frac{k_S^4}{48\pi} [1 + \cos^2(2\psi_0)] V^2 \left( \frac{\delta\mu}{\mu_0} \right)^2, \quad (\text{B.45})$$

$$\sigma_\mu^{ShSv} = \frac{k_S^4}{120\pi} [2 + 5 \cos^2(\psi_0)] V^2 \left( \frac{\delta\mu}{\mu_0} \right)^2, \quad (\text{B.46})$$

$$\sigma_\mu^{ShSh} = \frac{k_S^4}{24\pi} [1 + \sin^2(\psi_0)] V^2 \left( \frac{\delta\mu}{\mu_0} \right)^2, \quad (\text{B.47})$$

660 and

$$\tilde{\sigma}_\mu^{PSv} = \frac{\beta_0 k_S^2 k_P^2}{15\pi\alpha_0} V^2 \left( \frac{\delta\mu}{\mu_0} \right)^2, \quad (\text{B.48})$$

$$\tilde{\sigma}_\mu^{PSh} = \frac{\beta_0 k_S^2 k_P^2}{15\pi\alpha_0} V^2 \left( \frac{\delta\mu}{\mu_0} \right)^2, \quad (\text{B.49})$$

$$\tilde{\sigma}_\mu^{SvSv} = \frac{5k_S^4}{72\pi} V^2 \left( \frac{\delta\mu}{\mu_0} \right)^2, \quad (\text{B.50})$$

$$\tilde{\sigma}_\mu^{SvSh} = \frac{11k_S^4}{360\pi} V^2 \left( \frac{\delta\mu}{\mu_0} \right)^2, \quad (\text{B.51})$$

$$\tilde{\sigma}_\mu^{ShSv} = \frac{11k_S^4}{360\pi} V^2 \left( \frac{\delta\mu}{\mu_0} \right)^2, \quad (\text{B.52})$$

$$\tilde{\sigma}_\mu^{ShSh} = \frac{5k_S^4}{72\pi} V^2 \left( \frac{\delta\mu}{\mu_0} \right)^2. \quad (\text{B.53})$$

661 **B5 Validation**

We observe that

$$\frac{\sigma_{\rho}^{PSv} + \sigma_{\rho}^{PSh}}{\sigma_{\rho}^{SvP}} = \frac{\sigma_{\mu}^{PSv} + \sigma_{\mu}^{PSh}}{\sigma_{\mu}^{SvP}} = 2 \left( \frac{\alpha_0}{\beta_0} \right)^2. \quad (\text{B.54})$$

662 The above relationship agrees with previous research about the cross-section ratios between P and S waves (Aki 1992). We can further write

$$\sigma_{\rho}^{SS} = \sigma_{\rho}^{SvSv} + \sigma_{\rho}^{SvSh} = \sigma_{\rho}^{ShSv} + \sigma_{\rho}^{ShSh} = \frac{k_S^4}{6\pi} V^2 \left( \frac{\delta\rho}{\rho_0} \right)^2, \quad (\text{B.55})$$

$$\sigma_{\mu}^{SS} = \sigma_{\mu}^{SvSv} + \sigma_{\mu}^{SvSh} = \sigma_{\mu}^{ShSv} + \sigma_{\mu}^{ShSh} = \frac{k_S^4}{10\pi} V^2 \left( \frac{\delta\rho}{\rho_0} \right)^2. \quad (\text{B.56})$$

663 We observe that the two body-wave expressions above, along with the expressions of  $\sigma^{PP}, \sigma^{SvP},$   
664  $\sigma^{ShP}$  and  $\sigma^{PSv} + \sigma^{PSh}$  due to  $\delta\lambda/\delta\rho/\delta\mu$  are the same as the body-wave cross-section formulas  
665 in Margerin et al. (2000). Notice that the cross sections here are not averaged along incident  
666 angles.

667 **APPENDIX C: EQUIPARTITION FROM THE DENSITY OF STATE**

668 A basic principle in multiple scattering theory is equipartition. It stipulates that the correla-  
669 tion function of a diffuse field is proportional to the imaginary part of the Green's function  
670 of the underlying wave equation. The trace of the imaginary part of the local Green's func-  
671 tion is proportional to the (local) density of states (DOS) that counts all possible modes of  
672 propagation. Hence, the energy partitioning among different propagation modes in the diffuse  
673 regime can be obtained from the DOS. Formally, the DOS can be written as

$$\text{DOS} = -\frac{2\omega}{\pi} \text{Tr} \text{Im}G(\mathbf{x}, \mathbf{x}; \omega) = 2\omega \sum_n \delta(\omega^2 - \lambda_n) |\phi_n(\mathbf{x})|^2 \quad (\text{C.1})$$

674 for positive angular frequency  $\omega$ . In the last equality, the index  $n$  runs over all possible  
675 eigenmodes of the elastodynamic operator  $L = -\alpha^2 \nabla \nabla \cdot + \beta^2 \nabla \times \nabla \times$  with eigenvalues  $\lambda_n$  and  
676 displacement eigenfunction  $\phi_n$ . Notice that using  $\lambda$  to represent eigenvalues is custom in the  
677 DOS theory and we only use this representation in this appendix. These eigenfunctions must  
678 be normalized in the sense of the scalar product  $\langle \phi_n | \phi'_n \rangle = \int d^3r \phi_n(\mathbf{x}) \phi'_n(\mathbf{x})^* = \delta_{n,n'}$ . In our  
679 application, the index  $n$  will be continuous and all discrete sums become integrals as shown  
680 below. The eigenfunctions of the operator  $L$  in an elastic halfspace bounded by a free surface  
681 are plane Rayleigh wave and body-wave modes composed of an incident (normalized) plane  
682 wave of a given polarization (P/Sv/Sh) together with its reflections. A rigorous diagonalization  
683 of the operator  $L$  in a halfspace bounded by a free surface can be found in Sécher (1998) and

684 more details about the eigenvalues and eigenfunctions can be found in Margerin (2009). We  
 685 will examine the contributions of the different types of waves to the DOS using a classical  
 686 seismological approach in this section.

687 We first compute the DOS per unit surface for Rayleigh waves by integrating Equation C.1  
 688 over depth. Taking into account that a Rayleigh-wave eigenmode with horizontal wavevector  
 689  $(k_x, k_y)$  is associated to the eigenvalue  $\lambda = c_r^2(k_x^2 + k_y^2)$  and the normalization condition, we  
 690 find:

$$\begin{aligned} N_R &= 2\omega \int_{-\infty}^{+\infty} dk_x \int_{-\infty}^{+\infty} dk_y \frac{\delta(\omega^2 - c_r^2(k_x^2 + k_y^2))}{(2\pi)^2}, \\ &= \frac{\omega}{2\pi c_R^2}. \end{aligned} \quad (\text{C.2})$$

691 In the first line of Equation C.2, the factor  $(2\pi)^{-2}$  inside the integral is inherited from the  
 692 normalization condition for plane waves in 2-D. Note that  $N_R$  is a DOS per unit surface per  
 693 unit frequency.

694 Let us now examine the case for Sh waves. From the basic analysis of free-surface reflection,  
 695 we know that an Sh eigenfunction is of the form:

$$\phi_{Sh}(\mathbf{x}) = \frac{(e^{-iqz} + e^{iqz})e^{i(k_x x + k_y y)}}{(2\pi)^{3/2}} \mathbf{e}^{Sh}, \quad (\text{C.3})$$

696 which corresponds to the sum of an incident and a reflected plane wave with horizontal  
 697 unit polarization vector  $\mathbf{e}^{Sh}$  in the direction  $(k_y, -k_x, 0)$ . We take the vertical axis oriented  
 698 positively downward, so that a wavenumber  $-q < 0$  (i.e. positive  $q$ ) represents a up-going  
 699 wave. The eigenvalue associated to  $\phi_{Sh}$  is  $\lambda = \beta_0^2(k_x^2 + k_y^2 + q^2)$  and the prefactor  $(2\pi)^{-3/2}$   
 700 guarantees that the eigenfunction is correctly normalized. The squared modulus  $|\phi_{Sh}|^2$  is of  
 701 the form  $2 + 2 \cos 2qz$  and presents oscillations (i.e.  $\cos 2qz$ ) due to the interference between  
 702 upgoing and downgoing waves. As these interferences are not taken into account in our model,  
 703 we average the DOS over depth to disentangle the upgoing and downgoing waves. Reporting  
 704 the result:

$$\langle |\phi_{Sh}(\mathbf{x})|^2 \rangle_z = \frac{2}{(2\pi)^3} \quad (\text{C.4})$$

705 into the DOS definition yields:

$$\begin{aligned} \langle N_{Sh} \rangle_z &= 2\omega \int_0^{+\infty} dq \int_{-\infty}^{+\infty} dk_x \int_{-\infty}^{+\infty} dk_y \frac{2\delta(\omega^2 - \beta_0^2(q^2 + k_x^2 + k_y^2))}{(2\pi)^3} \\ &= \frac{\omega^2}{2\pi^2 \beta_0^3}, \end{aligned} \quad (\text{C.5})$$

706 where  $\langle \rangle_z$  denotes the depth average. In Equation C.5, the integral runs over positive  $q$  to

707 represent all possible incident (upgoing) plane Sh waves. The  $\delta$  function naturally selects only  
 708 those plane waves that satisfy the dispersion relation at frequency  $\omega$ .

709 The case of P and Sv waves is more complex than the above as these two waves are coupled  
 710 at the free-surface reflection. Thus, a part of the Sv DOS comes from converted P waves at  
 711 the free surface and vice-versa. A P eigenmode may be written as:

$$\phi_P(\mathbf{x}) = \frac{e^{i(k_x x + k_y y)}}{(2\pi)^{3/2}} (e^{-iq_p z} \mathbf{e}^P + \dot{P} \dot{P} e^{iq_p z} \mathbf{e}_r^P + \dot{P} \dot{S} e^{iq_s z} \mathbf{e}_r^{Sv}), \quad (\text{C.6})$$

712 where  $\mathbf{e}^P$ ,  $\mathbf{e}_r^P$  and  $\mathbf{e}_r^{Sv}$  are unit polarization vectors in the directions  $(k_x, k_y, -q_p)$ ,  $(k_x, k_y, q_p)$   
 713 and  $(-q_s, -q_s, k_x + k_y)$ , respectively. The first two polarizations are longitudinal and the  
 714 last one is transverse. The corresponding eigenvalue is  $\lambda = \alpha_0^2(k_x^2 + k_y^2 + q_p^2)$ . The vertical S  
 715 wavenumber is determined by  $q_s = \sqrt{\alpha_0^2(k_x^2 + k_y^2 + q_p^2)/\beta_0^2 - k_x^2 - k_y^2}$  and is always positive.  
 716 For the reflection coefficients, we use the standard notations from Aki & Richards (2002).  
 717 When we consider the quantity  $|\phi_P(\mathbf{x})|^2$ , cross terms involving  $P$  and  $S$  waves appear. Since  
 718 these terms are oscillatory, they cancel out when the squared eigenfunction is averaged over  
 719 depth, which in turn disentangles the P and S contributions:

$$\langle |\phi_P(\mathbf{x})|^2 \rangle_z = \frac{(1 + |\dot{P}\dot{P}|^2 + |\dot{P}\dot{S}|^2)}{(2\pi)^3} \quad (\text{C.7})$$

720 Eigenmodes for incident Sv waves have the form:

$$\phi_{Sv}(\mathbf{x}) = \frac{e^{i(k_x x + k_y y)}}{(2\pi)^{3/2}} (e^{-iq_s z} \mathbf{e}^{Sv} + \dot{S} \dot{S} e^{iq_s z} \mathbf{e}_r^{Sv} + \dot{S} \dot{P} e^{iq_p z} \mathbf{e}_r^P) \quad (\text{C.8})$$

721 where the corresponding eigenvalue is  $\lambda = \beta_0^2(k_x^2 + k_y^2 + q_s^2)$ , the definition of the polarization  
 722 vectors is similar as above, and the vertical P wavenumber  $q_p = \sqrt{\beta_0^2(k_x^2 + k_y^2 + q_s^2)/\alpha_0^2 - k_x^2 - k_y^2}$ .  
 723 Note that  $q_p$  may be pure imaginary when the incident angle of Sv waves is post critical for  
 724 the SP conversion. However, when averaged over depth, these evanescent  $P$  contributions van-  
 725 ish, so that we may consider the propagating regime only. This is in line with our numerical  
 726 approach where evanescent waves are neglected. The relation equivalent to Equation C.7 is  
 727 given by

$$\langle |\phi_{Sv}(\mathbf{x})|^2 \rangle_z = \frac{(1 + |\dot{S}\dot{S}|^2 + |\dot{S}\dot{P}|^2)}{(2\pi)^3}. \quad (\text{C.9})$$

728 Let us now collect all the terms that contribute to the DOS of Sv waves. These are the incident  
 729 and reflected S waves in Equation C.9 as well as the P to S conversions in Equation C.7 which

730 yields:

$$\begin{aligned} \langle N_{Sv} \rangle_z = & 2\omega \int_0^{+\infty} dq_s \int_{-\infty}^{+\infty} dk_x \int_{-\infty}^{+\infty} dk_y \frac{\delta(\omega^2 - \beta_0^2(q_s^2 + k_x^2 + k_y^2))}{(2\pi)^3} (1 + |\dot{S}\dot{S}|^2), \\ & + 2\omega \int_0^{+\infty} dq_p \int_{-\infty}^{+\infty} dk_x \int_{-\infty}^{+\infty} dk_y \frac{\delta(\omega^2 - \alpha_0^2(q_p^2 + k_x^2 + k_y^2))}{(2\pi)^3} |\dot{P}\dot{S}|^2. \end{aligned} \quad (\text{C.10})$$

731 Integrating over  $q$  and using polar coordinates for the horizontal wavenumbers integrals, we  
732 get:

$$\langle N_{Sv} \rangle_z = \frac{\omega}{4\pi^2} \left( \int_0^{\omega/\beta_0} \frac{(1 + |\dot{S}\dot{S}|^2)kdk}{\beta_0^2 \sqrt{\omega^2/\beta_0^2 - k^2}} + \int_0^{\omega/\alpha_0} \frac{|\dot{P}\dot{S}|^2 kdk}{\alpha_0^2 \sqrt{\omega^2/\alpha_0^2 - k^2}} \right). \quad (\text{C.11})$$

733 We now make the substitution  $k \rightarrow \omega \sin j / \beta_0$ :

$$\langle N_{Sv} \rangle_z = \frac{\omega^2}{4\pi^2 \beta_0^3} \left( \int_0^{\pi/2} (1 + |\dot{S}\dot{S}|^2) \sin j dj + \int_0^{j_c} \frac{\beta_0 |\dot{P}\dot{S}|^2 \sin j \cos j dj}{\alpha_0 \cos i} \right), \quad (\text{C.12})$$

734 where  $\sin i / \alpha_0 = \sin j / \beta_0$  and  $j_c$  is the critical angle of incidence of Sv waves for S-P con-  
735 versions. We now introduce additional relations: (1) Symmetry:  $\beta_0 \cos j \dot{P}\dot{S} = \alpha_0 \cos i \dot{S}\dot{P}$ ; (2)  
736 Energy conservation:  $|\dot{S}\dot{S}|^2 + |\dot{S}\dot{P}|^2 \alpha_0 \cos i / \beta_0 \cos j = 1$  for  $j \leq j_c$  and  $|\dot{S}\dot{S}|^2 = 1$  for  $j > j_c$ .  
737 Taking these elements into account, we arrive at the result:

$$\langle N_{Sv} \rangle_z = \frac{\omega^2}{2\pi^2 \beta_0^3}. \quad (\text{C.13})$$

738 A similar treatment applied to P waves gives:

$$\langle N_P \rangle_z = \frac{\omega^2}{2\pi^2 \alpha_0^3}. \quad (\text{C.14})$$

739 These results generalize the theoretical equipartition ratios to the case of a halfspace with a  
740 free surface. We observe that the ratios between  $N_R$  and  $\langle N_P \rangle_z$ ,  $\langle N_{Sv} \rangle_z$  and  $\langle N_{Sh} \rangle_z$  are the  
741 same as in Equations 17, 18 and 19.

## 742 APPENDIX D: PROBABILITY DISTRIBUTION OF BODY WAVE 743 INJECTION AT DEPTH IN RAYLEIGH-TO-BODY-WAVE SCATTERING

744 Rayleigh waves exist simultaneously at all depths at a given time while body waves exist  
745 only at a well-defined depth. Thus in the Monte Carlo simulation, we need 2D coordinate  
746 information (i.e.  $x$  and  $y$ ) to indicate the position of a Rayleigh wave and need 3D coordinate  
747 information (i.e.  $x$ ,  $y$  and  $z$ ) for the body-wave position. For RB scattering, the scattered body  
748 wave shares the same 2D position as the incident Rayleigh wave, but we have to add a depth  
749 ( $z$ ) to the body wave (i.e. inject the body wave at a depth).

750 We interpret  $\sigma^{RB}$  as the probability distribution of RB scattering at depth. We generate

751 a possible depth for the scattered body wave (i.e. realizations of the distribution) using in-  
 752 verse transform sampling. This sampling method requires the cumulative distribution function  
 753 (CDF) of  $\sigma^{RB}$  and a random number (*rand*) uniformly distributed from 0 to 1. We then find  
 754 a depth ( $z_s$ ) which satisfies

$$CDF(z_s) = \frac{\int_0^{z_s} \sigma^{RB} dz}{\int_0^\infty \sigma^{RB} dz} = rand. \quad (D.1)$$

755 The depth ( $z_s$ ) is the scattered body-wave depth. For example, in RSh scattering (Equa-  
 756 tion 11), we write the CDF as

$$CDF(z_s) = \frac{\int_0^{z_s} \sigma_\rho^{RSh} dz}{\int_0^\infty \sigma_\rho^{RSh} dz} = \frac{\int_0^{z_s} r_1^2(z, \omega) dz}{\int_0^\infty r_1^2(z, \omega) dz}, \quad (D.2)$$

757 where  $\frac{r_1^2(z, \omega)}{\int_0^\infty r_1^2 dz}$  is the probability distribution function (PDF) for the RSh scattering at depth  
 758 (Figure D1). The main part of the PDF is distributed between the one Rayleigh-wave wave-  
 759 length depth and the surface, and the CDF value is already close to 1 at the one wavelength  
 760 depth. Thus the scattering depth will be mostly distributed within one wavelength from the  
 761 surface. In practice, we do not compute the integral in the Monte Carlo simulations ( $\int_0^{z_s} \sigma^{RB} dz$   
 762 in Equation D.1), but instead calculate the CDF at some depths (*zvec* in Algorithm 4) prior  
 763 to the Monte Carlo simulation and then interpolate the depth ( $z$ ) during the simulation (Al-  
 764 gorithm 4). In the simulation, we choose the parameters about the depths as:  $Dz = 0.1$  and  
 765  $zmax = 10$ .

## 766 APPENDIX E: GENERATING SCATTERING AZIMUTHS AND 767 COLATITUDES

768 We determine the type of scattered wave based on the cross sections of all possible scattered  
 769 waves, and we use the cross section of the scattered wave to determine the scattering azimuth  
 770 and colatitude. In calculating a cross section, we integrate the squared scattered-wave ampli-  
 771 tudes along all possible scattering azimuths and colatitudes (e.g. Equation 8). A scattering  
 772 azimuth (colatitude) contributing more to the integral means that more scattered-wave energy  
 773 will be distributed at the azimuth (colatitude), which means the scattered wave will propagate  
 774 at the azimuth (colatitude) with a higher probability. Thus we interpret the integrand (e.g. in  
 775 Equation 8) as the PDF of scattering azimuth (colatitude). Following the same logic in Ap-  
 776 pendix D, we use inverse transform sampling to generate scattering azimuths and colatitudes.  
 777 For example, in ShR scattering, we only need the scattering azimuth and then write the PDF

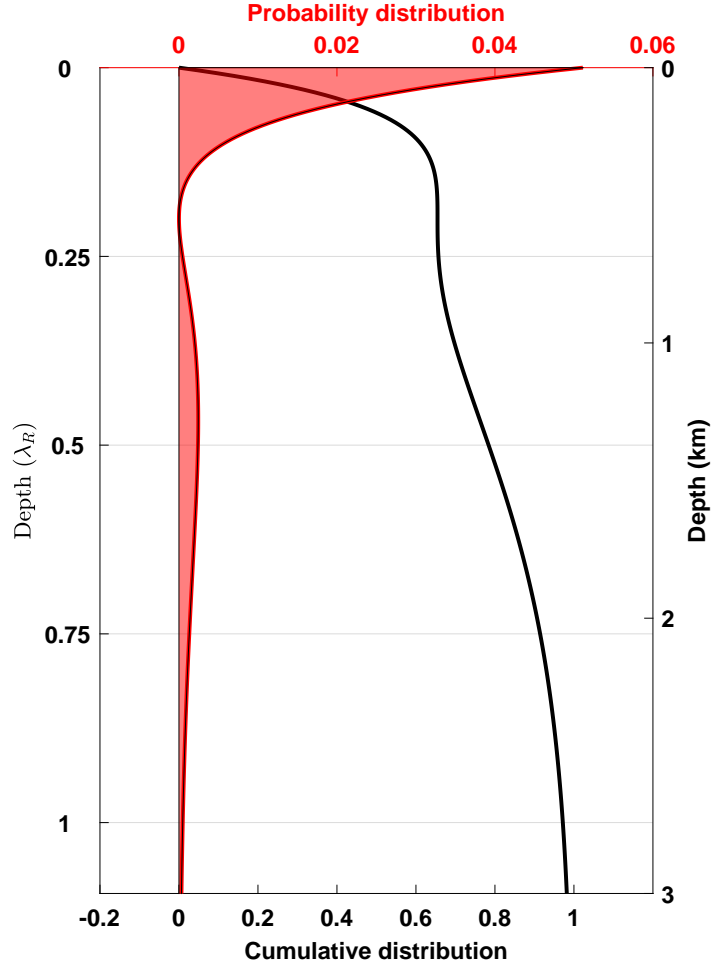


**Figure D1.** The probability and cumulative distributions of RSh scattering with depth.

778 of scattering azimuth as

$$PDF(\xi_1) = \frac{\sum_m |A_{m,\rho}^{ShR}|^2}{\int_0^{2\pi} \sum_m |A_{m,\rho}^{ShR}|^2 d\xi_1} = \frac{\sin^2 \xi_1}{\int_0^{2\pi} \sin^2 \xi_1 d\xi_1} = \frac{\sin^2 \xi_1}{\pi}. \quad (E.1)$$

779 We observe that the scattering azimuth is more likely to be  $\pi/2$  and  $3\pi/2$  deg (90 and 270  
 780 degree in Figure E1a), the azimuths orthogonal to the incident wave. No scattered Rayleigh  
 781 waves are expected at 0 or  $\pi$  (180 degree) for an incident Sh wave. These observations fit our  
 782 physical expectation in Section 2.2. We calculate the CDF based on Equation E.1, generate a  
 783 random number (*rand*) uniformly distributed from 0 to 1, and generate  $\xi_1$ , where  $CDF(\xi_1) =$   
 784 *rand*. We use this same approach to generate random scattering azimuths for other scattering  
 785 (e.g. the PR and SvR scattering).

786 For scattered body waves we need to generate both scattering azimuth and colatitude.

787 For example, in RSh scattering, the PDF of scattering azimuth ( $\xi_1$ ) and colatitude ( $\psi_1$ ) is

$$PDF(\xi_1, \psi_1) = \frac{\sum_m |A_{m,\rho}^{RSh}|^2 \sin \psi_1}{\int_0^\pi \int_0^{2\pi} \sum_m |A_{m,\rho}^{RSh}|^2 d\xi_1 d\psi_1} = \frac{\sin^2 \xi_1 \sin \psi_1}{\int_0^\pi \int_0^{2\pi} \sin^2 \xi_1 \sin \psi_1 d\xi_1 d\psi_1} = \frac{\sin^2 \xi_1 \sin \psi_1}{2\pi}, \quad (E.2)$$

788 where  $\sin \psi_1$  is due to the 2D spherical surface integrals in the total intensity of scattered Sh  
 789 waves. This PDF is independent of scattering depth, and in the PDF  $\xi_1$  and  $\psi_1$  are independent  
 790 (Figure E1b). Thus we generate the random azimuth and colatitude independently. Following  
 791 the approach in last paragraph, we generate a random azimuth. Using inverse transform  
 792 sampling and the PDF for the colatitude (i.e.  $\sin \psi_1$ ), we derive that the CDF for  $\psi_1$  is  $\cos \psi_1$ .  
 793 Thus we generate a random angle by calculating  $\cos^{-1}$  of a random number from a uniform  
 794 distribution between -1 and 1.

795 Notice that  $\psi_1$  and  $\xi_1$  are not required to be independent as in RP scattering. In such  
 796 a case, we need to generate a random azimuth and colatitude simultaneously. We write the  
 797 PDF for the two parameters in the RP scattering as:

$$PDF(\xi_1, \psi_1, z_s) = \frac{\sum_m |A_{m,\rho}^{RP}|^2 \sin \psi_1}{\int_0^\pi \int_0^{2\pi} \sum_m |A_{m,\rho}^{RP}|^2 \sin \psi_1 d\xi_1 d\psi_1} \quad (E.3)$$

$$= \frac{[r_1^2(z_s, \omega) \sin^2 \psi_1 \cos^2 \xi_1 + r_2^2(z_s, \omega) \cos^2 \psi_1] \sin \psi_1}{\int_0^\pi \int_0^{2\pi} [r_1^2(z_s, \omega) \sin^2 \psi_1 \cos^2 \xi_1 + r_2^2(z_s, \omega) \cos^2 \psi_1] \sin \psi_1 d\xi_1 d\psi_1}. \quad (E.4)$$

798 We observe that the distribution also depends on the scattering depth ( $z_s$ , Figure E1c and  
 799 E1d). In this case, we first determine  $z_s$  (Section D) and then find an azimuth and angle  
 800 ( $\xi_{1,s}$  and  $\psi_{1,s}$ ) which satisfy  $\int_0^{\xi_{1,s}} \int_0^{\psi_{1,s}} PDF d\xi_1 d\psi_1 = rand$  where  $rand$  is a random number  
 801 from a uniform distribution between 0 and 1. In practice, instead of calculating the integral  
 802 ( $\int_0^{\xi_{1,s}} \int_0^{\psi_{1,s}} PDF d\xi_1 d\psi_1$ ) in the simulations, we calculate a 2D CDF table for all possible  $\xi_{1,s}$   
 803 and  $\psi_{1,s}$  prior to the simulation; for a more accurate table, we use the cosine values for  
 804 scattering colatitudes (i.e.  $\cos \psi_1$ ) instead of the colatitudes (Algorithm 5). Notice that due  
 805 to the cosine, we do not need to incorporate  $\sin \psi_1$  in the PDF function like the one in the  
 806 right end of the numerator of Equation E.4.

## 807 APPENDIX F: BODY-WAVE ANGULAR DISTRIBUTIONS ON THE FREE 808 SURFACE

809 To illustrate how the free-surface boundary condition (FSBC) affects the simulation, we  
 810 present the incident and reflected body-wave angular distributions on the free surface under

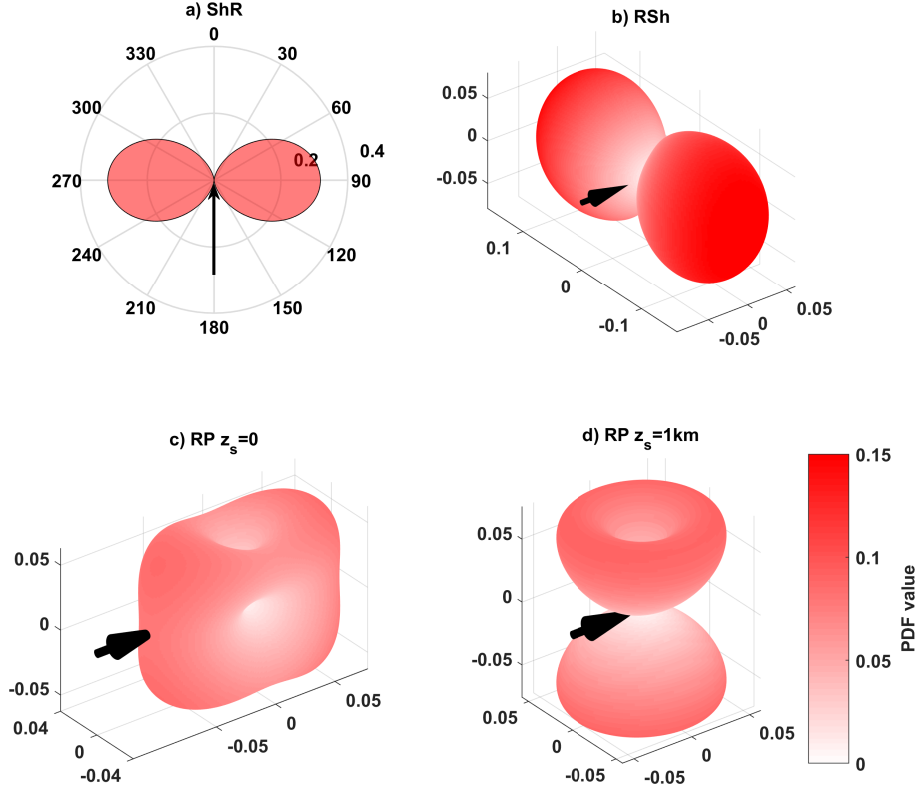


**Figure E1.** The PDFs for scattering azimuth (a) and scattering azimuth and colatitude (b, c and d). The radius in (a) is the PDF value. The color intensities in (b), (c) and (d) represent the PDF value. The black arrows represent the incident wave. The plot titles indicate the scattering type.

811 the mirror and mode-conversion FSBCs. Similar to Section 5.1, we divide all wave propagation  
 812 angles on the free surface (up-going and down-going) into 180 equal bins on the corresponding  
 813 cosine values from -1 to 1. We define the propagation angle ( $\psi_1$ ) as the angle between the wave  
 814 propagation direction and the down-going vertical direction (Figure 1). Thus  $\cos(\psi_1)$  values  
 815 for up-going/incident and down-going/reflected waves are negative and positive, respectively.  
 816 At each time step of the simulation, for each type of wave (i.e. P/Sv/Sh), we count how many  
 817 particles encounter the free surface and get reflected in each bin. We then calculate ratios

---

**Algorithm 5** Calculation of a 2D CDF table

---

```

dazi = pi/180; dcosang = 2/180;
intg = 0; CDF = zeros(360,180);
for iazi=0:359 do
    for icosang=0:179 do
        intg = intg + PDF((iazi+0.5)*dazi,(icosang+0.5)*dcosang)* dazi * dcosang;
        CDF(iazi+1,icosang+1) = intg;
    
```

---

818 between all the particle numbers and the P-wave particle number in the vertically up-going  
 819 bin, i.e.  $\cos(\psi_1) = -1$ . We average those ratios for the same wave type in a bin over a time  
 820 range such as first and last 50 Rayleigh-wave mean free times ( $\tau^R$ ) in the simulation. We  
 821 refer to those averaged ratios with respect to  $\cos(\psi_1)$  as the angular distribution for each  
 822 type of wave on the free surface (Figure F1). We observe that, in the first 50  $\tau^R$ , where  
 823 the simulations are not yet in equipartition, the two FSBCs perform differently and lead  
 824 to two different body-wave angular distributions (Figure F1a and F1c). However, after the  
 825 simulations reach equipartition (Figure F1b and F1d), the incident and reflected body-wave  
 826 distributions for the two FSBCs are identical and symmetric along the zero cosine value (i.e.  
 827 parallel to the free surface). These symmetric body-wave angular distributions fit Lambert's  
 828 cosine law,  $|\cos(\psi_1)|$ , as in the diffusion theory. The  $(\alpha/\beta)^2$  for Sh/Sv waves is the intensity  
 829 ratio between P and Sv/Sh, because we actually calculate intensity based on the number of  
 830 particles encountering/leaving a surface, instead of energies based on the number of parti-  
 831 cles in a space. Therefore we numerically demonstrate that the two FSBCs do not affect the  
 832 body-wave angular distribution on the free surface in the equipartition state.

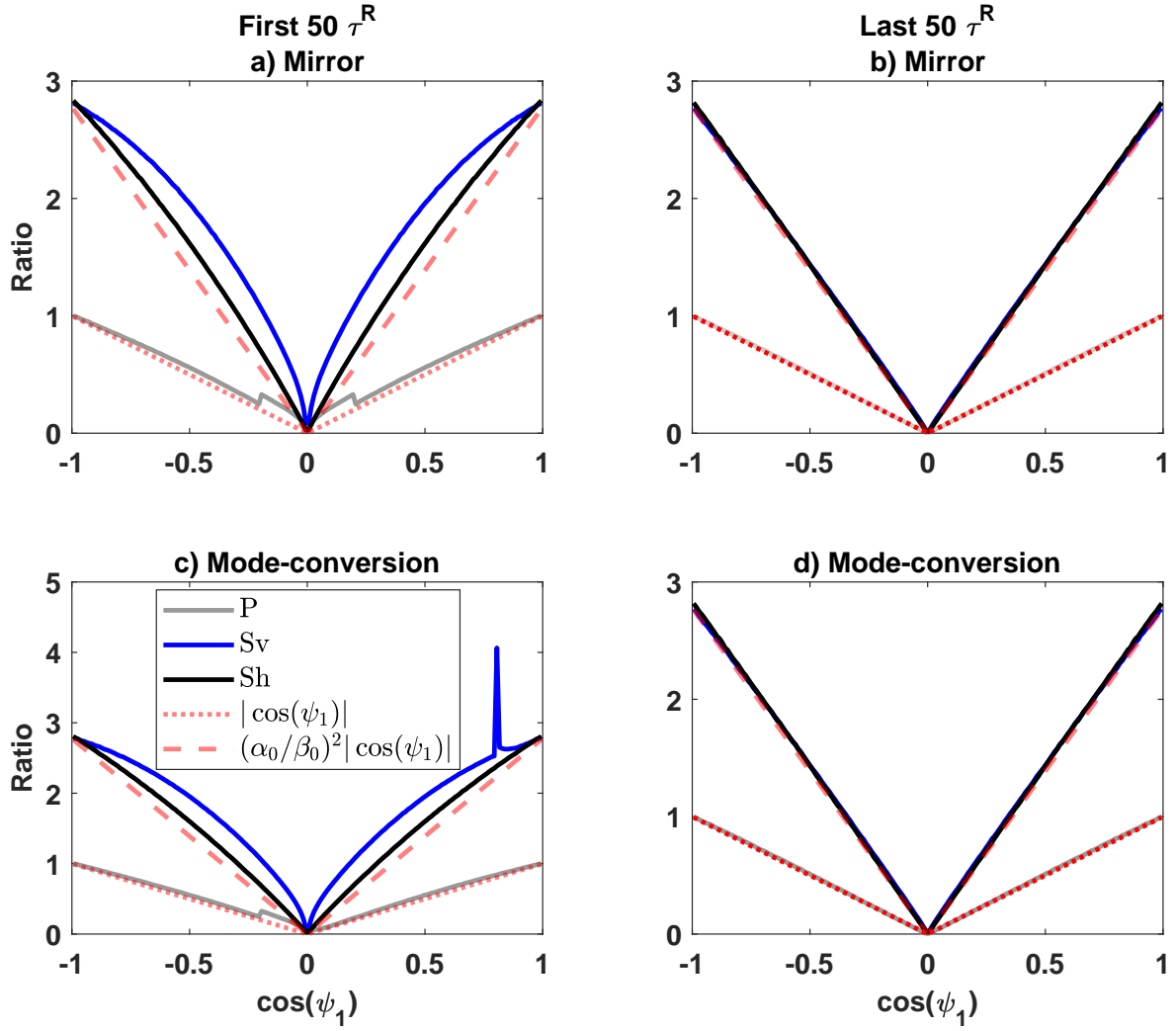


**Figure F1.** The body-wave angular distributions on the free surface under the mirror and mode-conversion FBSCs in the first and last 50 Rayleigh-wave mean free times. The peak in c) is due to the P-Sv-wave coupling on the free surface.